SECTION 2

MATERIALS

MACHINABILITY AND PHASE TRANSFORMATION STUDY OF NANOBAINITE STEELS

Chinmay Sonavane
Indian Institute of Technology
Madras, Tamilnadu, India

Dr. Ashwin Polishetty
Deakin University
Waurn Ponds, Victoria, Australia

Prof. Guy Littlefair
Deakin University
Waurn Ponds, Victoria, Australia

ABSTRACT

There is an increasing demand for high strength materials with the development of technology and critical applications. Nano materials are newly developed materials with extremely high strength for this purpose. Nanobainite is a dual phase material containing alternate layers of bainitic ferrite in nano dimensions and retained austenite. Nanobainite is produced by isothermally holding austenitized steel at a temperature of 200°C or less, depending on the chemical composition, for 6-10 days until bainite forms and then cooling to room temperature using austempering.

The experimental design consisted of face milling under 12 combinations of Depth of Cut (DOC)-1, 2 and 3mm; cutting speed-100 and 150m/min; constant feed-0.15mm/rev and coolant on/off. The machinability of the material is assessed by means of analysis, such as surface texture and microhardness. The assessment also involves microstructural comparisons before and after milling.

Future work involves quantifying the microstructural phase before and after milling using XRD. The results obtained are used to assess the most favorable condition to cut this new variety of steel.

INTRODUCTION

Steel is usually classified as a Fe-C alloy having a concentration of carbon in the range of 0.008 to 2.1%. The desired hardness level in Steel/Iron is obtained by varying the carbon (%) [1]. The hardness level can be altered by controlling the microstructural grain size through suitable heat treatment measures [2]. One such measure has given rise to a new form of high strength steel known as Nanobainite Steel. Nanobainite steel microstructure consists of alternate layers of bainitic ferrite laths surrounded by retained austenite. A carbon concentration gradient exists in the retained austenite which is verified by XRD techniques [3].

This has given the material an extended strength and enhanced mechanical properties. Hence, it is widely used in design applications requiring high strength. The microstructure of nanobainite steel is shown in Figure 1. As the transformation temperature increases, the diffusion of carbon from ferrite to austenite phase increases, which reduces the carbon concentration gradient ahead of the interface in retained austenite [3]. The lower the transformation temperature for the nanobainite steel formation, the stronger the material. This is because at lower temperature the nucleation rate is higher, which results in finer grains and eventually higher strength [4]. Nanobainite steels possess an excellent combination of strength and ductility along with grain refinement. Nanobainite steels exhibit an elongation of 21% for UTS above 2GPa.

Figure 1. Microstructure of Nanobainite steel

As silicon is a strong austenite stabilizer it gives an additional strength to the retained austenite at the transformation temperature which is also lowered due to the presence of excess Si [5] . The bainite transformation temperature decreases with the amount of carbon and other alloying elements in the material [5]. The transformation in nanobainite steel is formed by diffusionless transformation in the form of subunits. The transformation reaction stops when the carbon concentration in the retained austenite reaches the (T_o) curve as per the phase diagram. The ductility of nanobainite steel reduces on reducing the transformation temperature. The T_o curve is the locus of all points on the Fe-Fe_3C phase diagram, where austenite and ferrite of the same composition have same gibbs free energy [5]. The T_o curve for steels shifts depending on the mole fraction of the carbon added[6] as shown in Figure 2 below. The transformation of austenite to bainite is an isothermal transformation [7].

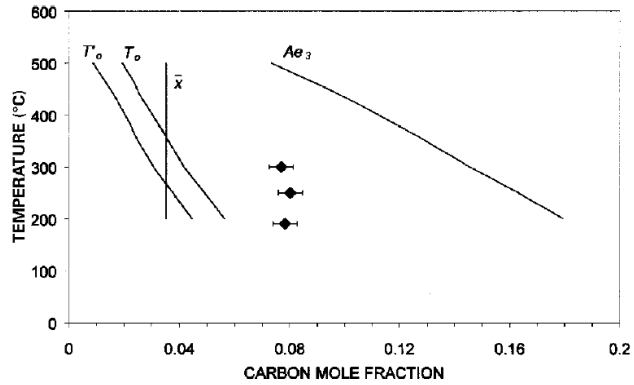

Figure 2. Dependence of To curve on mole fraction of carbon for steels

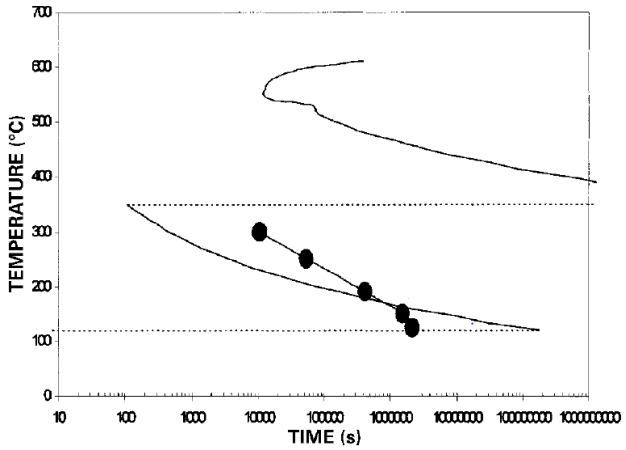

Figure 3. Calculated T-T-T curve for nanobainite steel: points in the graph indicate start and end of transformation

The time taken for transformation is calculated using the Time-Temperature-Transformation (T-T-T) diagram for steels as shown in Figure 3 above. The heat treatment for production of nanobainite steel depends on this diagram [7]. The nanobainite steels get distorted on quenching. The distortion depends immensely on the cooling rate employed for the production of that steel. These distortions are accommodated by the contraction of retained austenite due to stress relaxation [8]. Wear characteristics of nanobainite steels have been studied. The wear resistance of nanobainite is affected by transformation temperature, refined microstructure, TRIP effect. The nanobainite steels develop micro cracks on friction wear [9].

This research aims at studying the machinability of nanobainite steels, as machining results in phase transformations, which have an impact on the material properties. Hence, it is important to study the machinability, as it predicts the performance of the material in service.

PRODUCTION OF NANOBAINITE STEEL

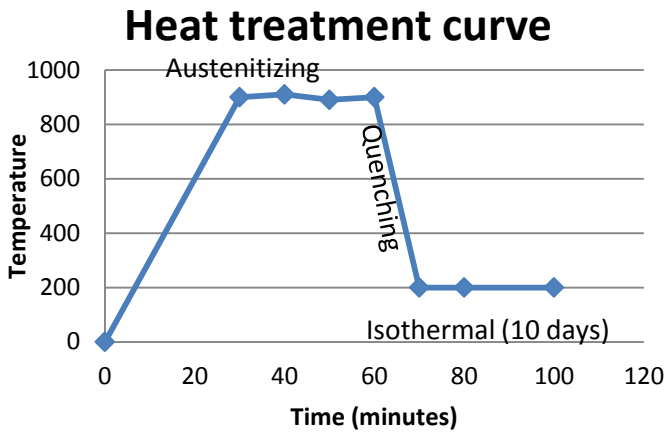

Figure 4. Heat treatment of nanobainite steel

The nanobainite steel used in this research is produced by austenitising steel at 900°C for 45 minutes, followed by isothermally holding the sample in a salt bath maintained at 200°C for 10 days. This is followed by an austempering operation. The heat treatment process is shown in Figure 4 [10].

CHEMICAL COMPOSITION OF NANOBAINITE STEEL

The chemical composition of nanobainite steel was evaluated using spectrometry. The elemental analysis is given in Table 1.

Table 1. Chemical composition

Element	Fe	Si	Mn	C	Cr	Cu	Ni
wt(%)	94.7	2.6	0.80	0.70	0.48	0.22	0.2

MACHINABILITY OF NANOBAINITE STEEL

The machinability of a material is defined as the ease with which the material is removed with decreased cutting force and by the tool wear that is observed during a machining process that obtains the desired surface finish. The machinability of nanobainite steel is very important, since the material's performance is evaluated by machining parameters like surface texture and microhardness. Machining results in phase changes of retained austenite to martensite in the presence of coolant by TRIP effect [7, 11]; this is evident by the microhardness measurements. This is a very important tool used for designing of a nanobainite structure for critical applications.

EXPERIMENTAL DESIGN

The experimental design consists of conducting milling trials at constant feed rate, 0.15mm/rev; variable speed-150 and 100 m/min; coolant on/off and variable DoC-1, 2 and 3mm. These trials are followed by tests of the surface roughness, by metallography and by microhardness tests.

SURFACE ROUGHNESS

Surface roughness is defined as the amount of material removed in the direction perpendicular to machining along the depth of the sample. It is measured in µm. The surface roughness analysis is done using Form Talysurf-50 analyser at a measurement speed of 1mm/s. The run-up length of the analyser was 0.3mm and the data length used was 5mm.

METALLOGRAPHY

The metallographic analysis includes mounting the sample using a poly-fast compact for 10 minutes. The poly-fast powder is sintered into a ceramic compact at 80°C during the initial stages of sintering and 180°C during the final stages. This is followed by polishing the sample using an electronic polisher for 10 min.

Figure 5. Nanobainite microstructure after machining

Finally, vella's reagent (2gr of Picric Acid+5ml HCl+100ml Ethanol) is used to etch the bulk nanobainite sample followed by ethanol cleansing in order to observe the microstructure. The microstructure seen after the metallography is shown in Figure 5.

MICROHARDNESS TEST

Microstructural analysis is done using an FM700 testing machine. The test is performed at 300grams of load for 10 seconds. The indenter used is a square base diamond pyramid indenter with an apical angle of 136°. In the microhardness test the length of indentation is measured and converted to the resultant Vickers hardness value. The microhardness test is performed as per the ASTM E-384 standard. The schematic of the microhardness test is shown in Figure 6.

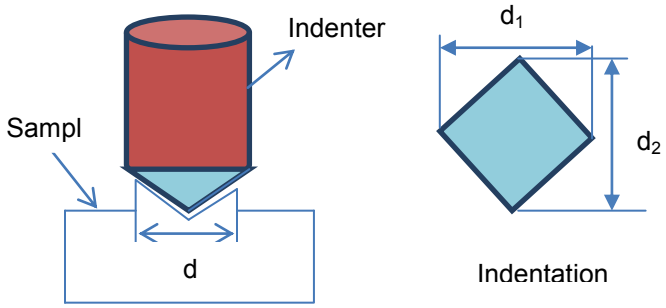

Figure 6. Schematic of Vickers Microhardness Test

RESULTS AND DISCUSSION

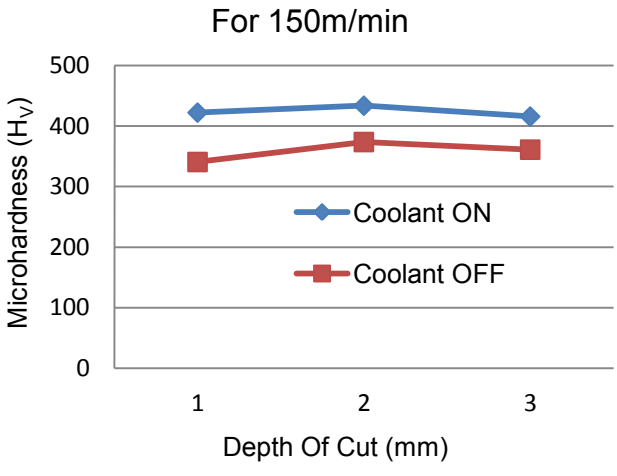

(A)

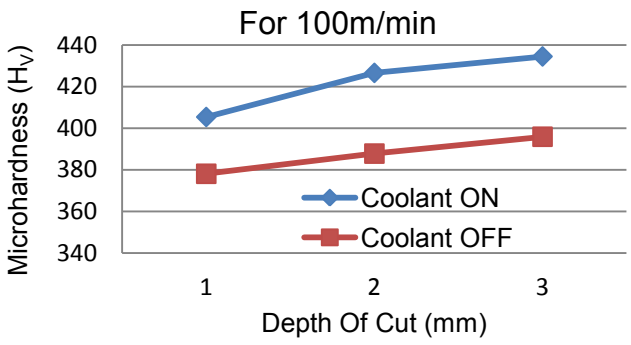

(B)

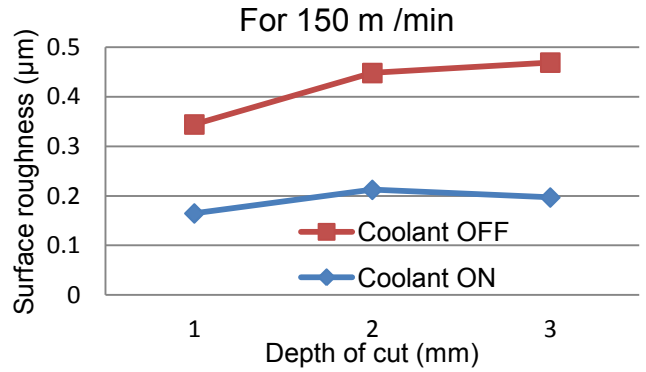

(C)

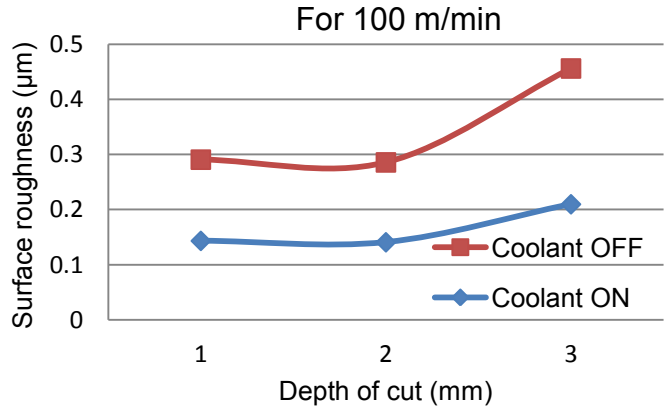

(D)

Figure 7. (A) Microhardness comparison between dry and wet machining at cutting speed of 150m/min, (B) Microhardness comparison between dry and wet machining at cutting speed of 100m/min, (C) Surface roughness comparison between dry and wet machining at cutting speed of 150 m/min, (D) Surface roughness comparison between dry and wet machining at cutting speed of 100 m/min

The machinability, as seen from the surface roughness plots in Figure 7, is better for the coolant OFF conditions rather than the coolant ON, since the surface roughness is greater in case of the former compared to the latter due to the thermal softening effect of the workpiece. This means lower cutting force is required to remove material in the coolant OFF condition compared to the coolant ON condition. Therefore we expect the material to be soft when machined under coolant OFF conditions, which is evident from the microhardness comparison plots for different machining speeds as well as the cooling conditions. In the case of the coolant OFF condition, the temperature of the sample is increasing with the machining speed along with the M_s temperature as the machining proceeds. Therefore, higher strains are required for the retained austenite to transform into martensite at both machining speeds. Hence, there is no or very little phase transformation in the case of coolant OFF condition; hence the material is softer. This is evident from the microhardness plots for the two machining speeds. In the case of the coolant ON condition, due to the presence of the coolant, the temperature of the sample remains almost constant, while the M_s temperature increases.

Hence, lower strains are required for the austenite to transform into martensite. Hence, the retained austenite transforms into martensite by TRIP (transformation induced plasticity) effect. Hence, the material is harder in this case which is evident from the microhardness plots for coolant ON condition. The machinability in this case is poorer than in the coolant OFF condition, since the amount of material removed in the direction perpendicular to machining is less due to the hardness of the material. This TRIP effect occurs at the point of intersection of sample temperature and the $M_s$temperature curve in the temperature v/s strain diagram for iron.

CONCLUSIONS

From the above discussion it is clear that the machinability obtained in case of coolant OFF condition is better than that obtained in the coolant ON condition. This is because the material is softer in the former case than the latter due to thermal softening effect and TRIP effect. The microhardness of nanobainite steel is higher in the coolant ON condition compared to the coolant OFF condition. This is because of the likely extent of phase transformation occurring in the material in the presence of the coolant. Therefore, appropriate material should be designed and machined to achieve the desired performance in service.

REFERENCES

[1] R. Abbaschian and R. E. Red-Hill, *Physical Metallurgy Principles*.

[2] D. A. Porter, *et al.*, *Phase Transformations in Metals and Alloys*, Third ed.: CRC Press, 2009.

[3] H. K. D. H. Bhadeshia, "Nanostructured Bainite," *The Royal Society*, vol. 466, p. 16, 2010.

[4] H. K. D. H. Bhadeshia, *et al.*, "Low Temperature Bainite," *Journal De Physique IV,* vol. 112, pp. 285-288, 2003.

[5] F. G. Caballero and H. K. D. H. Bhadeshia, "Very Strong Bainite," *Current Opinion in Solid State and Materials Science,* p. 16, 2004.

[6] H. K. D. H. Bhadeshia, F. G. Caballero, K. J. A. Mawella, and D. G. Jones, and P. Brown, "Very strong low temperature bainite," *Material Science And Technology,* vol. 18, p. 6, 2002.

[7] F. G. Caballero, H. K. D. H. Bhadeshia and. C. Garcia–Mateo, "LOW TEMPERATURE BAINITE," *Journal de Physique IV,* vol. 112, pp. 285-288, 2003.

[8] H. Hueng, C.M. Amey, P.E.J. Rivera-Díaz-del-Castillo "Distortion in 100Cr6 and nanostructured bainite," *Materials And Design,* vol. 35, p. 6, 2012.

[9] E. V. A. Leiro, K.G.Sundin , B.Prakash , T.Sourmail, V.Smanio , F.G.Caballero , C. Garcia-Mateo , Roberto Elvira, "Wear of nano-structured carbide-free bainitic steels under dry rolling–slidingconditions," *Wear,* vol. 298-299, p. 6, 2013.

[10] Y. A. H. Beladi, I. Timokhina and P.D. Hodgson, "Crystallographic analysis of nanobainitic steels," *Scripta Materialia,* vol. 60, p. 4, 2009.

[11] J. L. Garin and R. L. Mannheim, "Strain-induced martensite in ADI alloys," *Journal of Material Processing Technology,* 2003.

ASME District F - Early Career Technical Conference Proceedings
ASME District F - Early Career Technical Conference, ASME District F – ECTC 2013
November 2 – 3, 2013 - Birmingham, Alabama USA

POLYACRYLONITRILE (PAN) - CARBON INTERMEDIATE MATERIALS: ELECTRICAL AND CHEMICAL PROPERTIES

Monsur Islam, Ritwik Bandyopadhyay
Bengal Engineering and Science University
Shibpur, West Bengal, India

Swati Sharma, Marc J Madou
University of California, Irvine
Irvine, CA, USA

ABSTRACT

Electrospinning of Polyacrylonitrile (PAN) followed by oxidation and pyrolysis is one of the most widely investigated techniques for the production of carbon nanofibers (CNFs). In this work, the chemical composition and electrical properties of electrospun PAN nanofibers pyrolyzed at various pyrolysis temperatures ranging from 300ºC to 900°C have been characterized. These nanofibers, composed of PAN-carbon intermediate materials, feature an increasing trend in terms of the electrical conductivity with a steep increase in the 600°C-700°C temperature range. An attempt has been made to correlate electrical properties with a change in chemical composition to the fabricated nanofibers.

Keywords: PAN, Carbon MEMS, Electrospinning, Pyrolysis, and Carbonization.

INTRODUCTION

Over the past two decades, carbon has received a lot of attention as a potential alternative to silicon for microfabrication devices such as ICs and micro- and nano-electromechanical systems (MEMS and NEMS) [1]. Carbon can be found in nature in a variety of allotropes such as diamond, graphite, glassy carbon and diamond-like carbon (DLC) [1, 4]. A number of these advanced carbon materials have been extensively researched for their excellent electrical and electrochemical properties desirable in many MEMS and NEMS applications. The properties of carbon differ widely depending on different crystal structure and surface morphology [4, 5]. For example, glassy carbon electrodes provide a wide electromechanical window with low-background currents at a relatively low cost [2]. Graphite and hard carbons are well known for their Li-ion battery applications because of their Li intercalation/ de-intercalation capacity [3]. In addition, a number of nanoforms of carbon such as carbon nanotubes (CNTs), nanoparticles and nanofibers (CNFs) are receiving tremendous attention both in fundamental research and for microelectronics application [4, 5].

Polymer derived carbon MEMS (CMEMS) and carbon NEMS (CNEMS) often feature a glassy carbon microstructure. Glassy carbon has both amorphous and crystalline carbon regions [5]. The interconnected crystalline, or graphite regions allow for electron transport in glassy carbon and render it suitable for electrical and electrochemical applications unlike other amorphous materials [5].

Photolithography followed by pyrolysis is the most common technique for CMEMS fabrication; however a hybrid of CMEMS and CNF can be utilized as a CNEMS device [5] for sensing applications. For high performance CNEMS, electrospun CNFs are much more suitable compared to any other existing alternatives such as CNTs or chemically grown CNFs due to the simplicity and scalable nature of the fabrication process. The technique also allows for pre-defining the position of these fibers on contacting electrodes of any design.

CNFs can be produced from electrospinning of many different types of precursors such as rayon [6], polyacrylonitrile (PAN) [6], SU8 [5] and pitch [6]. However, about 90% of all carbon fibers worldwide are still derived from PAN [6]. An ideal precursor polymer for obtaining electrically conductive CNFs through electrospinning requires high carbon content, high molecular weight and high degree of molecular orientation. PAN satisfies all these requirements [7, 9]. PAN molecules however, are not aromatic in the polymer form.

The heat treatment for the carbonization of PAN can be divided into three main reactions: (i) oxygen attack on the polymer chain and take up of oxygen by the polymer, (ii) dehydrogenation of the carbon backbone of the polymer and (iii) cyclization of the nitrile groups present in PAN [19].

In this context, it is important to note that PAN, unlike other carbonizing polymers such as SU8, does not contain any aromatic groups in its polymer backbone. In the oxidation or stabilization of the PAN fibers the polymer backbone takes up oxygen, which facilitates a free radical generation during the subsequent pyrolysis, i.e., the heat treatment above 300°C under an inert atmosphere. The free radicals generated catalyze the cyclization of the nitrile groups [10] and render the carbon atoms close enough to form C-C bonds when the N atoms from the nitrile groups are released. In another study by Ko *et al.* [8] it was suggested that the oxidation process lengthens and broadens the carbon basal planes in the polymer backbone, which results in carbon fibers with an increased tensile strength

that have longer continuous carbon chains. Goodhew *et al.* [20] performed a detailed chemical structure evolution analysis elucidating the carbonization mechanism of PAN. According to these authors, the release of H (intermolecular dehydrogenation) takes place between 400°C and 600°C, while denitrogenation occurs at temperatures higher than 600°C. The ladder molecules formed during the oxidation join to form bigger aromatic molecules by a dehydrogenation process. Denitrogenation combines these dehydrogenated molecules to yield long ribbon-like geometries to finally result in a glassy carbon. The dehydrogenation process followed by denitrogenation suggested by Goodhew *et al.* [20] is illustrated in Figure 1.

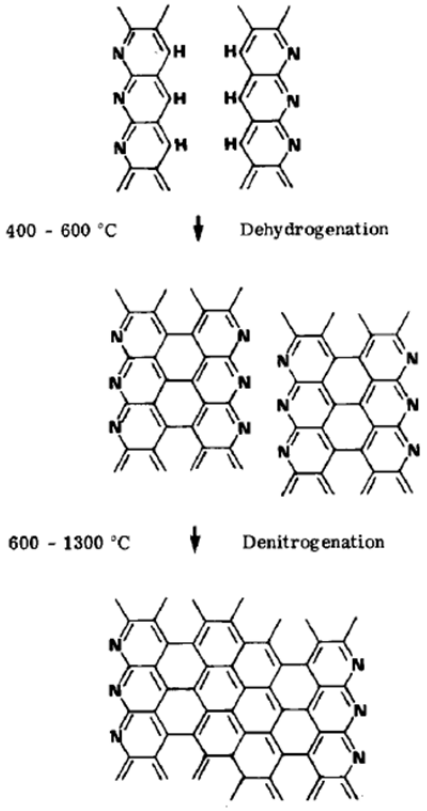

Figure 1. Dehydrogenation process followed by denitrogenation process during pyrolysis of PAN [20]

As described earlier, the carbonization of PAN fibers encompasses three basic steps: (i) thermoxidative stabilization (performed in air at 180ºC-280ºC), which forms a ladder-like molecular structure via nitrile; (ii) high temperature carbonization under an inert gas (≤900ºC) to exclude all non-carbon atoms and yield glassy carbon; (iii) an alternative "graphitization" (>2000ºC) to improve the orientation of the basal planes of the graphite sheets of glassy carbon [11, 13]. In this paper, we refer to the heat treatment carried out on oxidized PAN fibers as pyrolysis. Pyrolysis is most commonly performed at 900°C with a temperature ramp-up of <10°C/min in an inert environment (vacuum or under the flow of an inert gas such as nitrogen).

Most of the research on exploring the properties of PAN-carbon intermediate materials details chemical changes that occur during the carbonization, and are often correlated with the mechanical properties of the resulting nanofibers [7, 11]. However, not much attention has been paid to the electrical properties of the nanofibers derived from the PAN-carbon intermediate materials. In this contribution, the results of a detailed study of the pyrolysis of electrospun PAN nanofibers at final temperatures ranging from 300°C to 900°C is reported. The results include electrical conductivity tests correlated with the elemental analysis of these fibers. The fraction of the non-carbon components, namely H, O and N present in oxidized PAN decreases with the increase in pyrolysis temperatures, which leads to an increase in the electrical conductivity of the nanofiber material. Between 600°C and 700°C, a sudden increase in the conductivity was observed. Our results are supported by a discussion on the chemistry of the pyrolysis of PAN.

The pyrolysis process described above converts PAN, an insulator, into a highly conductive ultrapure glassy carbon. This implies that during the heat treatment there exist some intermediate PAN-carbon material(s) that might exhibit possible semiconductor characteristics and/or other functional properties.

EXPERIMENTAL PROCESS

MATERIALS

Commercially available PAN procured from Sigma Aldrich was used to fabricate PAN nanofibers. According to the manufacturer, the average molecular weight of the PAN was 150,000 MW. A research grade (99.8%) dimethylformamide (DMF) (Fisher Scientific) was used as the solvent and PAN solution. Silicon wafers coated with a 500 nm oxide layer were obtained from Noel Technologies (CA, USA).

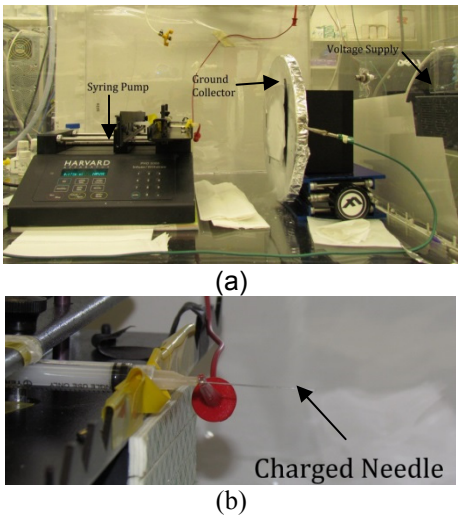

(a)

(b)

Figure 2. (a) Far field electrospinning set up for fabricating the PAN nanofibers (b) The charged needle tip which acts as a nozzle in electrospinning

METHODS

(i) FABRICATION OF PAN FIBERS

PAN nanofibers were produced by a far field electrospinning technique. Figure 2 illustrates the set up used for this purpose. Two different types of samples: bulk nanofibers balls (Figure 3) and nanofiber mats on SiO_2 coated silicon wafers were fabricated for elemental analysis and electrical resistance measurement respectively. For fabricating nanofiber balls, the fibers were collected on an aluminum foil and were peeled off.

(II) STABILIZATION AND PYROLYSIS

PAN nanofiber-balls on the aluminum foils and the PAN nanofiber mats on the silicon wafers were first oxidized at 220ºC temperature in a convection oven in air. The oxidized samples were pyrolyzed in an RD-G Furnace (RDWEBB company, Patent no: 5,987,053) at 300ºC, 400ºC, 450ºC, 500ºC, 600ºC, 700ºC, 800ºC and 900ºC. Figure 3 illustrates a color change in these nanofiber balls pyrolyzed at different temperatures. Images a and b are for the as prepared PAN nanofibers and the oxidized PAN nanofibers respectively.

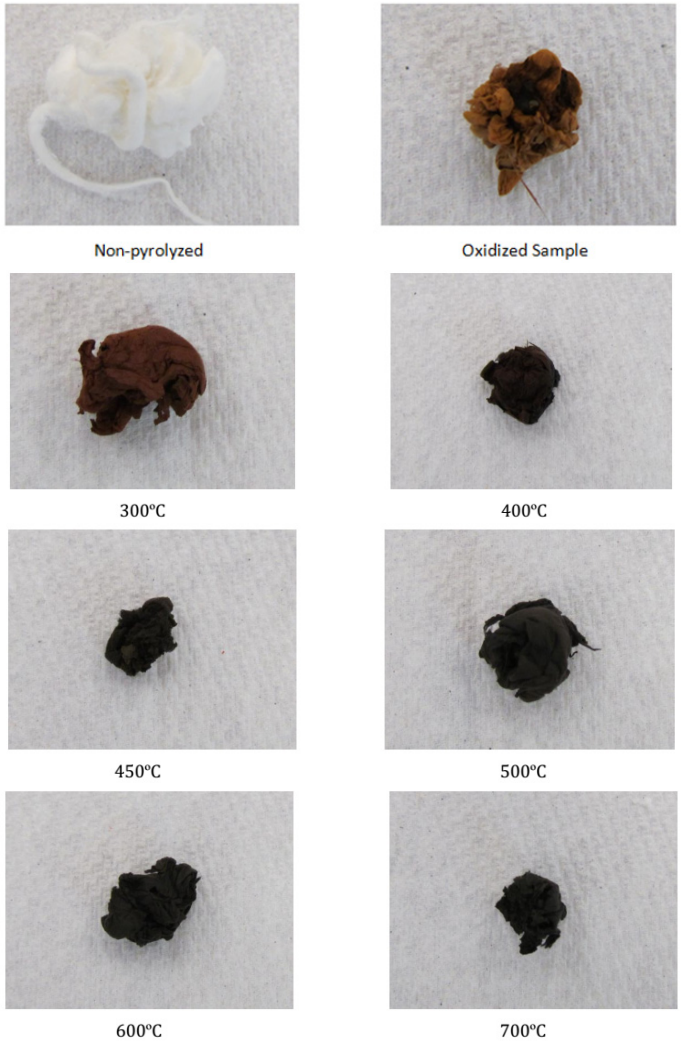

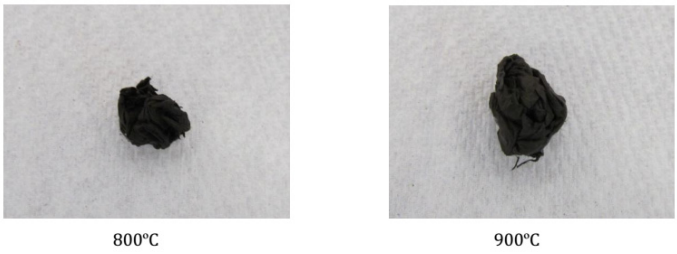

Figure 3. Electrospun PAN fibers after pyrolysis at different temperatures

RESULTS AND DISCUSSION

The electrical resistance of eight different nanofiber mats composed of PAN-carbon intermediate materials pyrolyzed in the range of 300°C - 900°C is measured by the four pin probe method. The electrical characterization was not carried out for PAN nanofibers without any oxidation or pyrolysis, since PAN is an insulator in the heat treatment. The results of the electrical characterization are listed in Table 1. Figure 4 shows a plot of these resistance values with respect to the pyrolysis temperatures.

TABLE 1: Resistances of the samples at various temperatures

Pyrolysis Temperature	Average Resistance
300ºC	$6.48 \times 10^8\ \Omega$
400ºC	$6.58 \times 10^8\ \Omega$
450ºC	$6.72 \times 10^8\ \Omega$
500ºC	$6.58 \times 10^8\ \Omega$
600ºC	$5.33 \times 10^8\ \Omega$
700ºC	$7.22 \times 10^4\ \Omega$
800ºC	$8.01 \times 10^3\ \Omega$
900ºC	$2.70 \times 10^3\ \Omega$

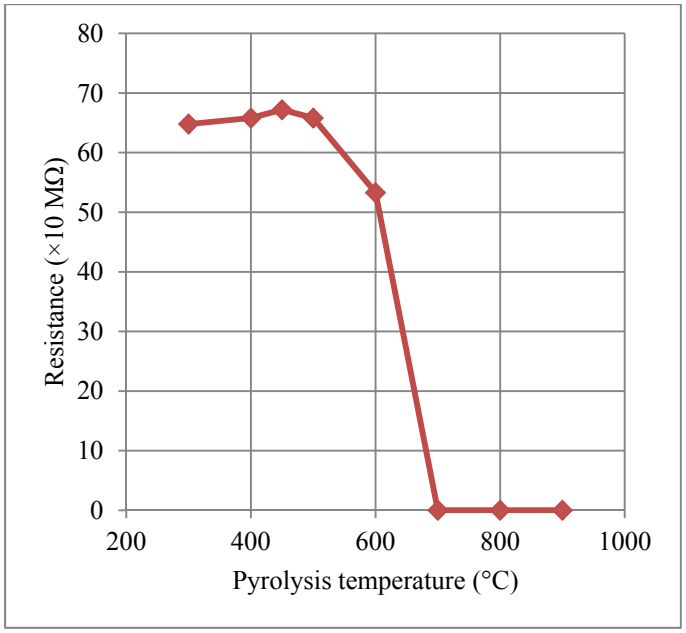

Figure 4. Electrical resistance of nanofiber mats composed of PAN-carbon intermediate materials obtained from pyrolysis at different temperature

It can be inferred from Figure 4 that the electrical resistance of the nanofibers decreases with an increase in the pyrolysis temperature between 450°C - 900°C. The first two data points; i.e., PAN pyrolyzed at 300°C and 400°C respectively, display only a slight difference in electrical resistance, and the resistance indeed increases with the highest resistance measured at 450°C. From this point the resistance drops rapidly as the pyrolysis temperatures are further increased between 600°C and 700ºC. After 700°C, there is no significant difference in the resistance. The difference in the resistance between 700ºC, 800ºC and 900ºC are comparatively less.

TABLE 2. Percentage of Carbon, Hydrogen, Nitrogen and Oxygen present in the nanofiber samples pyrolyzed at various temperature

Temperature	%C	%H	%N	%O
Not Pyrolyzed	65.46	4.43	24.85	6.25
300	62.31	3.57	20.84	10.97
400	63.97	3.03	20.23	9.63
450	66.09	2.88	21.72	7.21
500	66.48	2.09	19.49	10.87
600	69.47	1.52	18.19	7.48
700	71.88	1.19	17.89	6.17
800	74.99	0.78	13.26	6.44
900	80.63	0.58	7.47	5.63

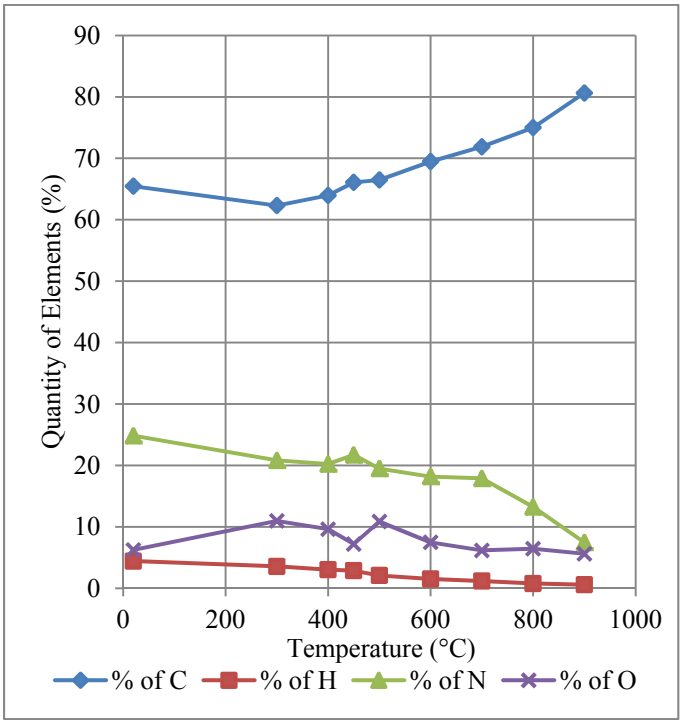

Figure 5. Graphical representation of the variation of C, H, N, O percentage w.r.t. temperature

A change in other physical properties of these pyrolyzed PAN nanofibers is also observed, such as the color of the pyrolyzed samples as the pyrolysis temperature is increased [Figure 3]. As the carbon content in the samples increases, it attains a more blackish color, which finally turns completely black after 700ºC. The color change of the samples with increasing temperature can be attributed to the chemistry of the pyrolysis process. An elemental analysis was carried out to determine the amount of non-carbon components present and a sequence to their release during pyrolysis. The result of the elemental analysis is given in Table 2.

As expected the fraction of carbon in the nanofibers increases with increasing pyrolysis temperature, while the fraction of the other elements i.e. H, N and O decreases. In the carbonization process stabilized precursor fibers are converted into glassy carbon. About 50% of the non-carbon elements usually get volatized in the form of methane, hydrogen, nitrogen, hydrogen cyanide, water, carbon dioxide, carbon monoxide, ammonia and other gases [14]. As a consequence, the material shrinks and the overall surface to volume ratio is enhanced, rendering these nanofibers more suitable for sensing applications. Nanofibers undergo shrinkage with the increase in pyrolysis temperature due to mass-loss. A representative scanning electron micrograph of PAN nanofibers before pyrolysis compared to a sample carbonized at 600°C is illustrated in Figure 6. The SEM micrograph confirms that the average diameter of the fibers is ~500 nm before pyrolysis and ~200 nm after carbonization at 600°C.

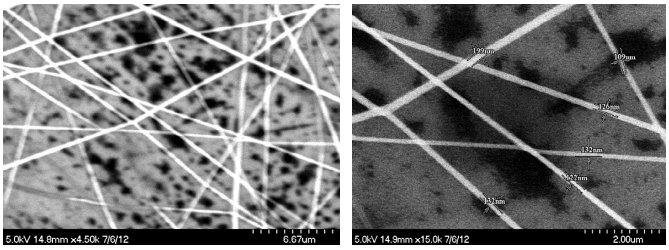

(a) (b)

Figure 6. SEM Pictures showing the size of the PAN fibers (a) before pyrolysis and (b) after pyrolysis at 600°C temperature for 60 minutes.

Figures 7 to 9 elucidate the chemistry of the carbonization of PAN. The initial chemical changes during the carbonization processes are illustrated in Figure 7 [7, 10]. When the fibers are further heated in an inert environment, the cross linking and aromatization reactions occur with gentle heat release [7, 10, 11]. The free radicals generated simultaneously cause rearrangement of the oxygen containing groups. The degree of aromatization can be increased at this stage, whereby carbon basal planes in the stabilized fibers begin to form and increase in dimension [7, 10, 11, 15].

The next stage of carbonization is the active pyrolysis stage in the region 450°C-550ºC, where large quantities of free radicals are yielded because of the large scale random rapture of linear molecular fibers segments [7, 10]. As the carbon content in the fiber increases, the carbon molecules begin to crosslink in small zones.

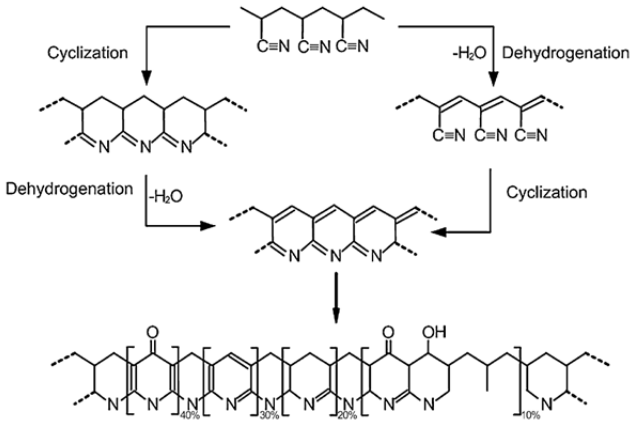

Figure 7. Proposed chemistry of preliminary stages of carbonization [13, 17, 18]

In the final stage (i.e. in the region of 550-700ºC), ladder polymer starts to crosslink into carbon basal planes to enhance aromatization [10] and form large networks of carbon basal planes. Above 700ºC in temperature, the number of cross-linked carbon basal plane increases, and the carbon tends to become more graphitic.

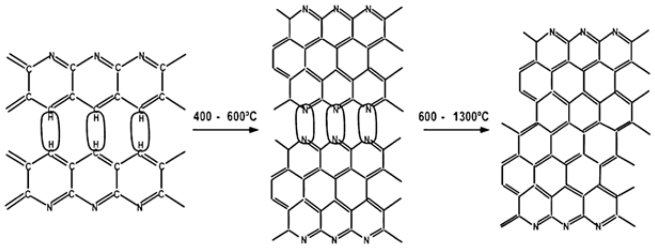

Figure 8. Proposed structure change of PAN precursor during pyrolysis [16]

At low temperatures (<500°C) H and N are removed in the form of HCN and NH_3. However, there is still some remaining N in the polymer that is released in the form of N_2 at elevated temperature (>500°C). During the oxidation of PAN, oxygen is absorbed within the sample as -C=O. Later at higher temperatures, oxygen escapes from these bonds as water vapor due to evolution of H_2O. The evolution of H_2O occurs due to the crosslinking between two monomer units of the adjacent ladder polymers, which is schematically represented in Figure 9 [13, 19]. This process starts at the temperature range 450°C-500°C and dominates the pyrolysis in the range 500°C - 700°C.

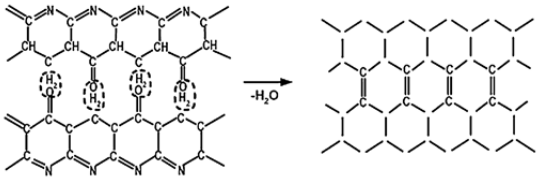

Figure 9. Mechanism of oxygen escape from ladder polymer in form of H_2O [13, 19]

As the formation of carbon basal planes increases and the graphitization process progresses with temperature, the carbon fibers become more conductive. Hence resistance of the samples reduces with the increase in temperature. Moreover removal of O also improves the electrical conductivity. Figure 10 illustrates the electrical resistance of PAN nanofiber mats with an increasing fraction of C fraction and decreasing fraction of O. This clearly indicates that an enhanced crystallininty and the removal of O significantly drop the resistance within the temperature range 500°C – 700°C.

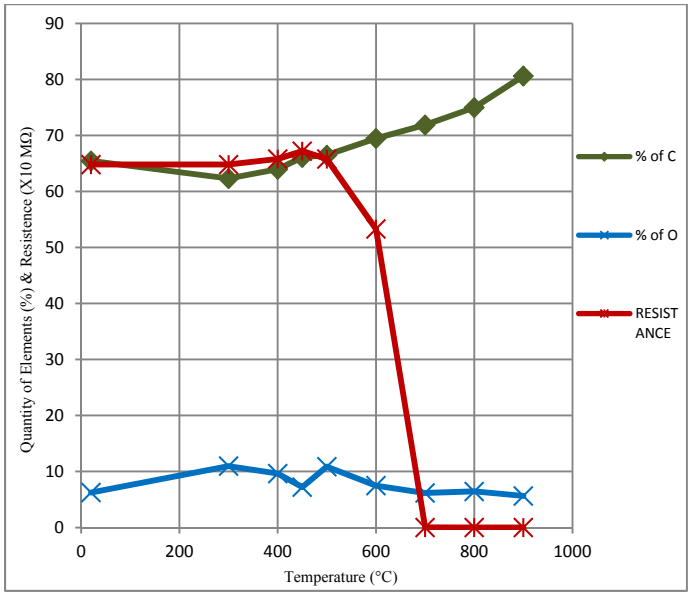

Figure 10. A graphical representation of contribution of percentage increase of carbon and percentage decrease of oxygen in decrease of resistance of PAN-carbon intermediate materials

CONCLUSION & FUTURE WORK

In this work, nanofibers composed of PAN-carbon intermediate materials were successfully fabricated and characterized. The results obtained here confirm that there is a sudden change in the electrical properties of the intermediate material between 600°C and 700°C. For the first time, a correlation between the electrical properties and elemental analysis data has been reported through this work. It can help the researchers in understanding the chemistry of the pyrolysis process and can help them to obtain nanofibers that can feature pre-defined electrical conductivity and chemical composition. This data can also be utilized for fine-tuning the pyrolysis process to yield glassy carbon with highly improved structural and chemical properties.

In previous research within our group we have successfully fabricated single suspended PAN and SU8 derived CNFs on CMEMS electrodes that can be utilized for sensing purposes [5]. The electrospun nanofibers composed of the PAN-carbon intermediate materials reported here can be integrated with a CMEMS platform in a similar fashion, which will allow for a wider choice of electrical properties and chemical composition of a nanofiber sensor material.

ACKNOWLEDGEMENTS

The authors of this report are very thankful to the Indo-US Centre for Research Excellence on Fabrionics (IUCREF) and the UC Irvine lab funds for providing the financial support and the research facilities for this project.

REFERENCES

[1] Madou, M., 2002, "Fundamentals of Microfabrication: The Science of Miniaturization", 2nd edition, CRC Press.

[2] Pocard, N.L., Alsmeyer, D.C., McCreery, R.L., Neenan, T.X., Callstrom, M.R., 1992, "Doped glassy carbon: a new material for electrocatalysis", J. Mater. Chem., Vol. 2 (8), pp. 771–784.

[3] Eesenhard, Jurgen, O. (Eds.), 1999. Handbook of Battery Materials. Wiley/VCH.

[4] Wang, C. and Madou, M, 2004, "From MEMS to NEMS with Carbon", Biosensors and Bioelectronics, Vol. 20, pp. 2181–2187.

[5] Sharma, S., Sharma, A., Cho, Y. K., Madou. M., 2012, "Increased Graphitization in Electrospun Single Suspended Carbon Nanowires Integrated with Carbon-MEMS and Carbon-NEMS Platforms", *ACS Applied Materials and Interfaces* ,Vol. 4 (1), pp. 34–39.

[6] Schwartz M, Encyclopedia of Materials, parts and finishes, 2nd edition, Boca Raton, Florida: CRC Press; 2002

[7] Yusof, N., and Ismail, A. F., 2012, "Post spinning and pyrolysis processes of polyacrylonitrile (PAN)-based carbonfiber and activated carbon fiber: A review", Journal of Analytical and Applied Pyrolysis, Vol. 93, pp. 1–13.

[8] Ko, T. H., and Day, T. C., 1994, "The effect on Pre-carbonisation on the properties of PAN-based Carbon Fibers", Polymer Composites, Vol. 15, No 6.

[9] Sutasinpromprae, J., Jitjaicham, S., Nithitanakul, M., Meechaisue, C., Supaphol, P., 2006, "Preparation and Characterization of Ultrafine Electrospun Polyacrylonitrile Fibers and Their Subsequent Pyrolysis to Carbon Fibers", Polymer International, Vol. 55, pp. 825–833.

[10] Jing, M., Wang, C., Wang, Q., Bai, Y., Zhu, B., 2007, "Chemical structure evolution and mechanism during pre-carbonization of PAN-based stabilized fiber in the temperature range of 350-600ºC", Journal of Polymer Degradation and Stability, Vol. 92, pp. 1737-1742.

[11] Lui, J., Wang, P. H., Li, R. Y., 1994," Continuous Carbonization of Polyacrylonitrile-Based Oxidized Fibers: Aspects on Mechanical Properties and Morphological Structure", Journal of Applied Polymer Science, Vol. 52, pp. 945-950.

[12] Desai, S., Netravali, A., Thompson, M., 2006, "Carbon Fibers as a Novel Material for High-Performance Microelectromechanical Systems (MEMS)", Journal of Micromechanics and Microengineering, Vol. 16, pp. 1403–1407.

[13] Rahaman, M. S. A., Ismail, A. F., Mustafa, A., 2007, "A Review on Heat Treatment on Polyacrylonitrile fiber", Polymer Degradation and Stability, Vol. 92, pp. 1421-1432.

[14] Edie, D. D., 1997, "The Effect of Processing on the Structure and Properties of Carbon Fibers", Carbon, Vol. 36, No 4, pp. 345-362.

[15] Ko, T. H., Li, C.H., 1995, "The influence of pre-carbonization on the properties of PAN based carbon fibers developed by two-stage continuous carbonization and air oxidation", Polym. Compos. Vol. 16, pp. 224–232.

[16] Zhu, D., Xu, C., Nakura, N., Matsuo, M., 2002, "Study of carbon films from PAN/VGCF composites by gelation/crystallization from solution", Carbon, Vol. 40(3), pp. 363-373.

[17] Wiles, K.B., 2002, “Determination of reactivity ratios for acrylonitrile/methylacrylate radical copolymerization via nonlinear methodologies using real time FTIR”, MSc thesis, Faculty of the Virginia Polytechnic Institute and State University: Blacksburg, Virginia.
[18] Bansal, R.C., Donnet, J.B., Stoeckli, F, 1988, Active carbon, New York: Marcel Dekker Inc.
[19] Manocha, L.M., Bahl, O.P., 1980, “Role of oxygen during thermal stabilization of PAN fibres” Fiber Sci Technology, Vol. 13(3), pp. 199-212.
[20] Goodhew, P.J., Clarke, A.J., Bailey, J.E., 1975, “Review of fabrication and properties of carbon-fibers”, Mater. Sci. Eng., Vol. 17, pp. 3–30.

MACHINABILITY ASSESSMENT OF TI-6AL-4V FOR AEROSPACE APPLICATIONS

Ashwin Polishetty,
Deakin University
Geelong, Victoria, Australia

Vignesh Manoharan
VIT University
Vellore, Tamilnadu, India

Guy Littlefair
Deakin University
Geelong, Victoria, Australia

Chinmay Sonavane
Indian Institute of Technology
Madras, Tamilnadu, India

ABSTRACT

Titanium alloy Ti-6Al-4V is the most commonly used titanium alloy in the aerospace and biomedical industries due to its superior material properties. An experimental investigation has been carried out to evaluate the machinability of high performance aerospace alloys (Ti-6Al-4V) to determine their in service performance characteristics based on different machining strategies. Nearly 80-90% of the titanium used in airframes is Ti-6Al-4V.

The experimental design consist of face milling Ti-6Al-4V at 12 different combinations of cutting parameters consisting of Depth Of Cut (DoC)- 1, 2 and 3 mm; speeds- 60 and 100 m/min; coolant on/off and at constant feed rate of 0.04mm/tooth. Post machining analysis consists of cutting force measurement, surface texture analysis and metallographic analysis. The future work consists of in-depth investigation into the phase transformational reactions during machining.

INTRODUCTION

The metallurgy of titanium and its base alloys have been intensely researched over last 50 years. Titanium has unique properties such has high strength to weight ratio, good resistance to corrosive environments. It can be used over a wide range of applications due to its superior material properties. It is a strong metal with little ductility, lustrous and metallic white in color. The relatively high melting point makes it useful as refractory material. Several superior properties, such as exceptional thermal resistance, high load bearing capacity and ability to resist corrosion, of these materials categorize them as super-alloy. Typical engineering applications of titanium alloys include the manufacture of cryogenic devices and aerospace components. Titanium is not widely used as aluminium or steel as it is an expensive metal. It is the seventh most abundant metal found on earth's crust. However, titanium is difficult to extract from its core, difficult to process and manufacture [1].

As the strength of the titanium is higher than the aluminum alloys, weight savings can be achieved when they replace aluminium despite the 60 percent higher density [1]. Titanium has low thermal conductivity; hence the heat generated by the cutting action does not dissipate quickly [2, 3].

Another property is strong alloying tendency or chemical reactivity with the most tool materials which causes rapid destruction of the cutting tool [2, 3].

LITERATURE REVIEW

Titanium exists in two crystallographic forms. At room temperature unalloyed titanium has a Hexagonal Close-Packed structure (HCP) crystal structure known as alpha phase. At 883^{o}C this transforms to a Body Centered Cubic (BCC) known as beta phase [1]. The microstructure of Ti-6Al-4V before machining is shown in figure 1. The most noted chemical property of titanium is excellent resistance to corrosion, it is almost as resistant as platinum. The metal cannot be melted in open air, since it burns before the melting point it is reached. So melting is only possible in an inert atmosphere or vacuum [4].

When machining any component it is essential to satisfy surface integrity requirements. However during machining and grinding operations, the surface of titanium alloys is easily damaged of their poor machinability [5]. Aerospace components are mainly manufactured from big stock material by removing huge amount of material. Sometimes the weight ratio of stock material to final product becomes more than 50. Casting is the main process to produce stock material.

The temperature gradient during cooling the huge casting of stock material generates residual stress. With the start of the machining process the residual stress starts to release and the machined part starts to distort [6, 7]. Aerospace components are generally made by removing huge amounts of scarf from big blocks of material. The near net shaping method is very difficult for most aerospace components due to complex physical shape, and high tolerance and good surface finish requirements [8]. Excellent examples of utilization of titanium because of volume constraints are the landing gear beams on the Boeing 747 and 757. The 747 beam is one of the largest titanium forgings produced. The preferable material for this

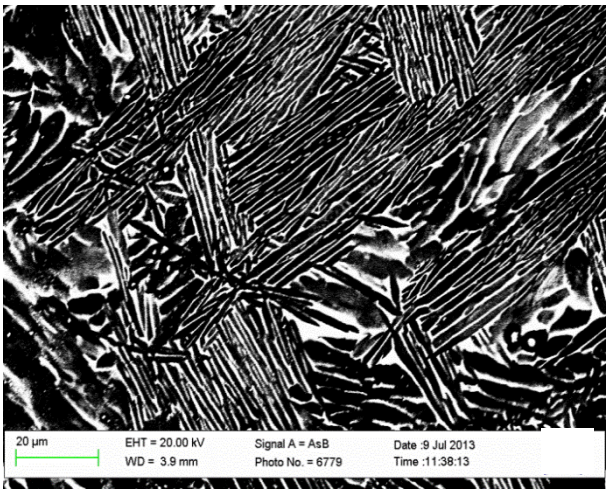

Figure 1. Ti-6Al-4V microstructure – before machining

application would have been an aluminium alloy, such as 7075, as the cost would be much lower. However, to carry the required loads, the machined aluminium component would not fit within the envelope of the wing. Steel could have been used, but it would have been heavier, owing to the higher density [9].

Ti-6Al-4V has been workhorse of the titanium industry and probably 80% - 90% of the titanium used on airframes has been this alloy. It is used in fuselage, nacelles, landing gear, wing and empennage. Cobalt–bound tungsten carbide cutting tools are widely accepted as the best tooling for machining Ti-6Al-4V. The higher strength of Ti-6Al-4V would permit reducing the wall thickness, enhancing the weight savings [9]. Vanadium (V) is added to pure Ti to reduce the β transition temperature for stabilizing the β phase, and aluminium (Al) is added to increase the β transition temperature. Ti–6Al–4V consists of 6 wt% of Al and 4 wt% V. The β transition temperature of this composition is 995 °C; beyond this temperature it is 100% β phase [10].

The chips are witnesses of physical and thermal phenomena happening during machining. Their study is fundamental for a better understanding of the cutting process as well as to improve the surface integrity of the machined part. It is generally agreed that during metal cutting practically all the deformation energy is transformed into heat on the tool cutting edge. Some heat is transferred by conduction to the uncut material ahead of the tool, affecting the surface integrity of the machined element. At lower cutting speeds the chips are often discontinuous, while the chip becomes serrated as the cutting speeds are increased. The greater the cutting speed, the higher will become the temperature in the primary deformation zone. The resistance to crack propagation to the tool tip direction increases with the cutting speed [11]. Chinmaya R. Dandekar et.al [12] carried out hybrid machining, assisted with laser. In laser assisted milling the workpiece material is heated and softens before entering cutting zone. Two to three fold tool life improvements over conventional machining are achieved for hybrid machining upto the speed of 200 m/ min as reported by the author. They established that by using the TiAlN coated tool in Laser Assisted Machining (LAM) and hybrid machining 30% to 40% of overall cost saving can be achieved. This reduced the specific cutting energy by up to 20% and the surface roughness by 30% as compared to conventional machining.

Titanium alloys are generally difficult to machine at cutting speeds over 30 m/min, with HSS steel tools and 60 m/min with cemented tungsten carbide tools. Other types of tool materials, including ceramic, diamond and cubic boron nitride are highly reactive with titanium alloys, and as a consequence are not used in the machining of these alloys [13].

Based on the hardness, many tools are able to machine titanium alloys. But most of the harder tools, available in the market are not suitable to machine these materials due to chemical affinity, which causes chemical wear in the cutting tool. Furthermore, chips weld easily on the tool to form a built up edge (BUE) [11]. When it comes to the design of the cutting tool for machining titanium both the low heat transfer rate and the low modulus of elasticity must be taken into consideration. To combat these constrains, high shear geometry must be incorporated. Both high helix angle and radial rake angles combine to create a higher effective rake or sheer plane [3]. High temperature strength, very low thermal conductivity, relatively low modulus of elasticity, high strain hardening, poor dislocation motion through the microstructure and high chemical reactivity play an important role in machining mechanism of these alloys [14].

EXPERIMENTAL DESIGN

The experimental design consists of two parts. First is the material characterization and the second and final part involves machining trials. Material characterization includes spectrometry analysis, tensile test, bulk hardness test and material characterization of Ti-6Al-4V. Post machining processes include surface roughness test, chip morphology and

Table 1. Chemical Composition of Ti-6Al-4V

Chemical Compounds	Percentage (By wt)
V	4.22
Al	5.48
Sn	0.0625
Zr	0.0028
Mo	0.005
C	0.369
Si	0.0222
Cr	0.0099
Ni	<0.0010
Fe	0.112
Cu	<0.02
Nb	0.0386
Ti	90.0

microstructure analysis of machined alloy. The various elements present and the chemical compositions of the Ti-6Al-4V (in wt %) examined by spectroscopic analysis are given in Table 1. The measured mechanical properties, such as bulk hardness, tensile strength of the Ti-6Al-4V alloy are shown in Table 2.

Table 2. Mechanical Properties of Ti-6Al-4V

Work material	Ti-6Al-4V
Ultimate tensile Strength (MPa)	887
Modulus of elasticity ($x10^6$ MPa)	11.3
Hardness (HRC/ 12mm/ 150 Kgf)	28-32

Table 3. Milling parameters of Ti-6Al-4V

Milling Trial No	DoC (mm)	Speed (m/min)	Coolant
1	3	60	Off
2	2	60	Off
3	1	60	Off
4	3	100	Off
5	2	100	Off
6	1	100	Off
7	3	60	On
8	2	60	On
9	1	60	On
10	3	100	On
11	2	100	On
12	1	100	On

The workpiece material used in all the experiments of machining was a bar of dimension 150mm X 50mm X 18mm alpha- beta titanium Ti-6Al-4V alloy. The Titanium block was machined with different combinations of milling parameters, and the resulting cutting forces were measured using a Kistler dynamometer 9257B in this project. The machining trials consist of face milling Ti-6Al-4V at 12 different combinations obtained from the cutting parameters consisting of DoC-1, 2 and 3mm; speeds-60 and 100m/min; coolant on/off and at constant feed rate of 0.03mm/tooth. Twelve different combinations of speed, DoC and coolant used for machining are shown in the Table 3.

Milling was carried out in a universal line 5-axis CNC machine manufactured by Spinner U-620. The tool used for milling was a coated solid carbide end mill of 12mm diameter containing four teeth, manufactured product of ISCAR-IC900. The coolant used was a phenol-2.8% which is mixed with water in ratio of 1:10. The dynamometer senses the forces induced during the machining and sends this information back in the form of electrical signals to the amplifier, which converts data that will be displayed in form of graph onto the computer. Dynoware software was used with the Kistler's dynamometer to study the cutting forces during machining operations. Post machining process consists of surface roughness analysis, microstructure analysis of the Ti-6Al-4V alloy. For easy handling of the small samples during polishing and microstructure analysis it was mounted. The cut samples were mounted with "Polyfast" material. Mounting was carried out in an automated mounting machine, where the sample was heated to a temperature of 180^{o}C, 25 bar pressure for about six minutes and then rapidly cooled with water for about two minutes.

The samples were then polished in automatic polishing machine manufactured by "Struers- Rotoforce4" with OPS grid sheet and OPS 80-20% solution for 30 minutes with force of 20N. Ultrasonic cleaner was used to remove all the particles sticking to the mounted samples. SEM "Supra – 55VP, ZEISS" was used to analyze the microstructure of the machined samples. The microscopic structure of the titanium alloy samples was compared with the original microstructure before machining. A surface roughness test of the machined titanium block was performed using a "Taylor Hobson – Form Talysurf" roughness testing machine. "Ultra" software was used along with machine, which gives the output in graph form on the computer. A stylus made up of a diamond edge was used to determine the surface roughness. Data length used for testing was 15 millimeters and run-up length is 1 mm/sec.

RESULTS AND DISCUSSION

The measured cutting forces during machining of Ti-6Al-4V alloy are plotted in form of a graph using Dynoware. The highest force was measured during wet machining operation with the large DoC and low feed rate. The lower the cutting forces involved, the better will be the productivity of machining. The higher the cutting forces, the higher will be the temperature flow in the tool, which rapidly causes the tool to failure in case of machining titanium alloy. One such graph obtained for 60m/min speed, 3mm DoC, dry machining is shown below in the Figure 2. Higher forces were recorded in case of wet machining when compared to dry machining; this is because of retardation of thermal softening of the workpiece by

the action of coolant. Cutting forces for dry and wet machining for DoC 3mm and 100 m/min speed is shown in figure 3.

From the experiment it has been studied that the tool wear is more in case of low speed machining compared with high speeds. The stress on the cutting edge also increases with the increase of cutting speeds due to the decrease of contact length and shear angle. It is noted that periods of large force fluctuations (dynamic force) occurred randomly during machining Ti-6Al-4V.

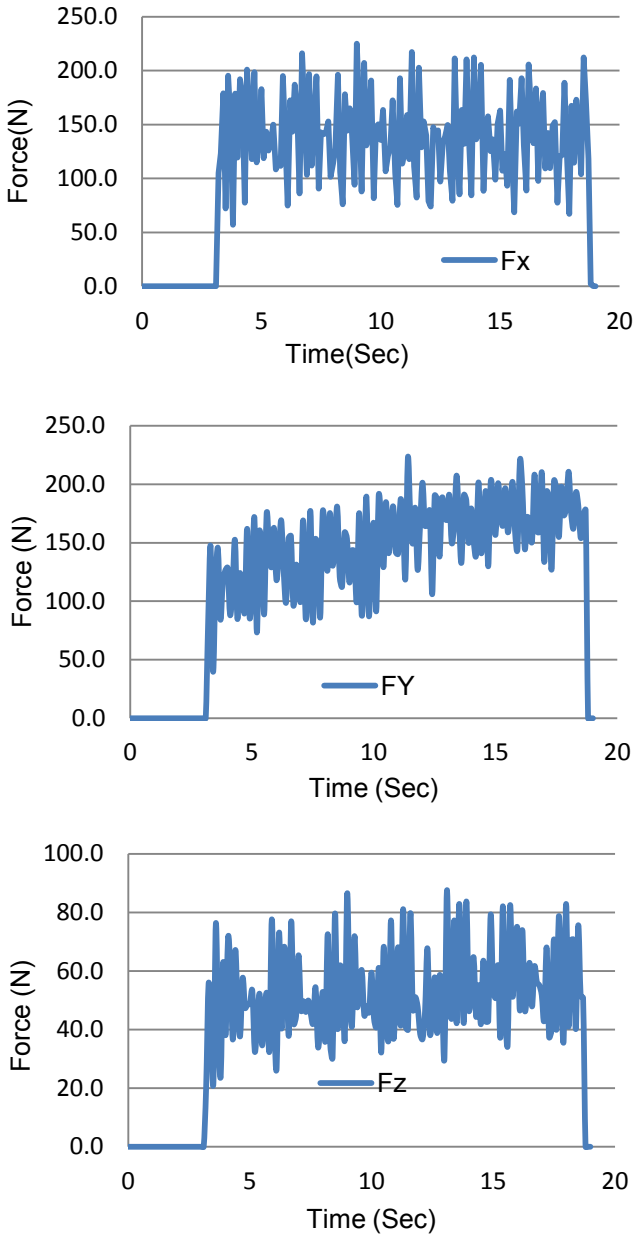

Figure 2. Cutting force in x, y and z axis for 3mm DoC, 60 m/min cutting speed

These fluctuations make the tool to vibrate, which would result in early tool failure. The fluctuations in cutting forces are evident more when the DoC is large and high cutting speed. Surface roughness for 60m/min and 100m/min, dry machining is shown in the figure 4. The surface roughness (R_a) value for 100m/min speed, dry machining is lower when compared to 60m/min, dry machining. That is, the high speed has better surface finish compared to low speed machining. Surface roughness values were compared between dry and wet machining operations as shown in the figure 5.

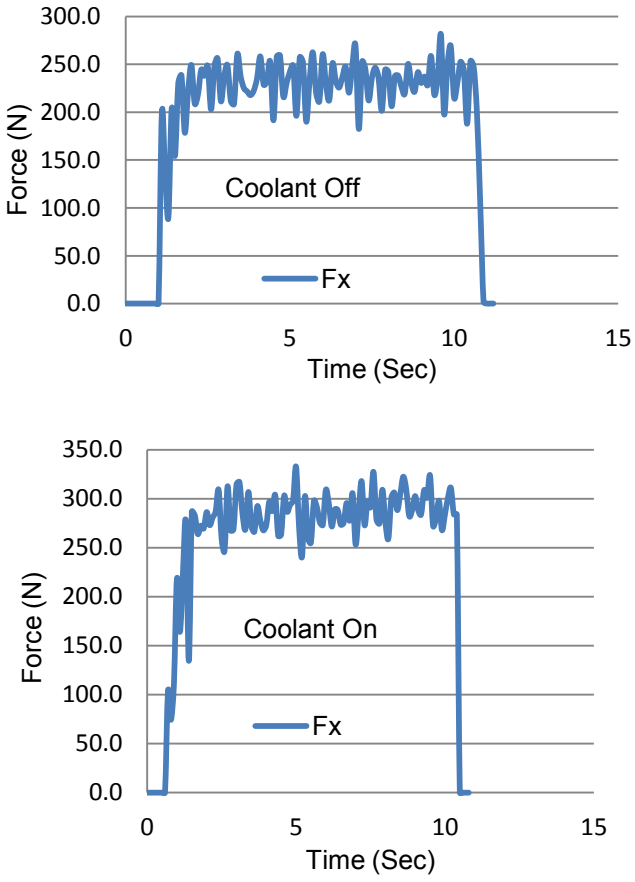

Figure 3. Cutting forces in x axis for DoC 3mm, cutting speed 100 m/min

When comparing the surface roughness of dry machining with wet machining operation, it can be said that wet machining has a fine surface roughness value. By the action of coolant the chemical reactivity of titanium to the tool surface is reduced and also the cutting temperature is decreased which give rise to better tool action onto the surface of the workpiece.

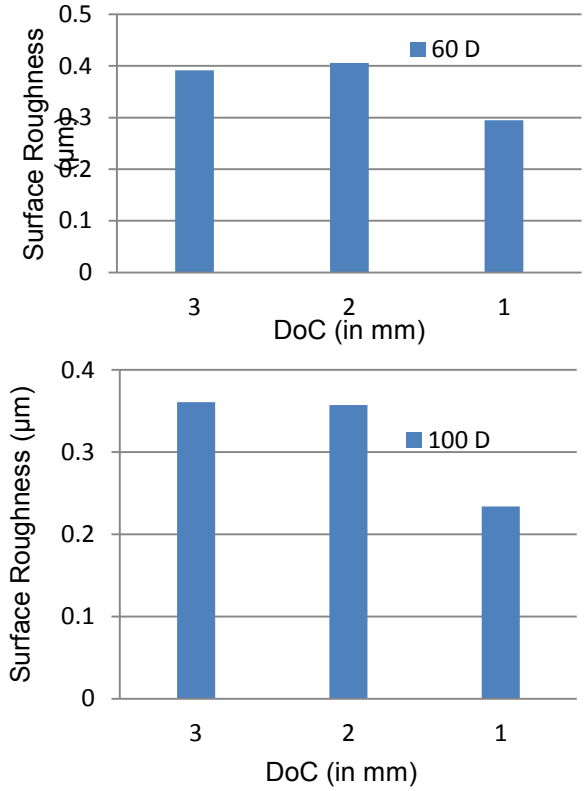

Figure 4. Cutting force in x, y and z axis for DoC 3mm, cutting speed 60 m/min

A sample of machined Ti-6Al-4V alloy has been examined in SEM for the microstructure analysis. A picture of a Ti-6Al-4V sample examined after machining under SEM is shown in the figure 6. The SEM test was undergone for the sample machined at a speed of 100m/min and 1 mm DoC, dry machining. When comparing the SEM microstructure with the original alloy microstructure, phase transformation of beta and alpha alloy is seen. It states that the Ti-6Al-4V alloy likely to be tempered after machining.

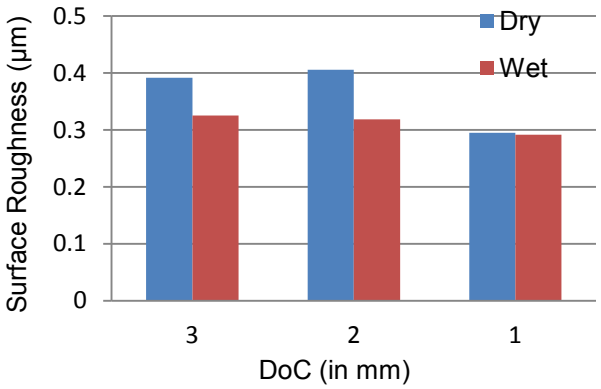

Figure 5. Surface roughness comparison between dry and wet machining for 100m/min cutting speed

Lamellar type light coloured alpha phase with dark coloured beta phase in between can be seen from the SEM microstructure of the machined sample. The mechanism of phase transformation in titanium during milling has to be studied in depth to improve the productivity in machining.

CONCLUSION

An experimental investigation was carried out to understand the machinability of the high performance aerospace alloys, which helps to improve the Ti-6Al-4V productivity in aerospace industries.

By conducting the orthogonal type end milling of Ti-6Al-4V alloy following results were concluded:

- Cutting forces in x, y, z axis increases as DoC increases and the cutting force is high for wet machining when compared to dry machining. By the application of coolant in machining the effect of thermal softening is reduced, which leads to higher cutting force. Therefore, reduction of cutting force in machining should be the aim to acquire higher productivity.
- Cutting forces measured while machining Ti-6Al-4V has force fluctuations, which is due to the higher strength of the workpiece material. These fluctuations in the cutting force produces higher tool wear.
- Cutting force is higher in case of high cutting speed compared to low cutting speed, which likely resulted in higher tool wear. Tool wear should be low enough to acquire high productivity. The maximum cutting forces was recorded at high cutting speed with large DoC.
- Surface roughness measurement showed that DoC-1mm produced lower surface roughness. This was achieved with high speed than the low speed with same DoC. This can be explained as that the specific cutting force needed to machine the material is more when cutting speed is high.
- Surface roughness for the Ti-6Al-4V material obtained by wet machining was low compared to the dry machining. The use of coolant in machining reduces the tool-workpiece temperature. Also the chemical affinity of titanium alloy to the tool is reduced with the use of coolant. So, fine surface texture was obtained when machining with the application of coolant.
- When examining the microstructure of the machined Ti-6Al-4V alloy under SEM, phase transformation in the microstructure is likely visible when compared with the original SEM microstructure. Lamellar type light coloured alpha phase was seen with dark coloured beta phase in between in SEM microstructure. This showed that the alloy has been likely tempered which resulted in lamellar like beta phase microstructure.
- Chemical affinity of titanium alloy to the tool was seen more when machining in dry conditions. This was reduced

in the case of wet machining, as the coolant washes away in between the tool-workpiece interface and the chips.

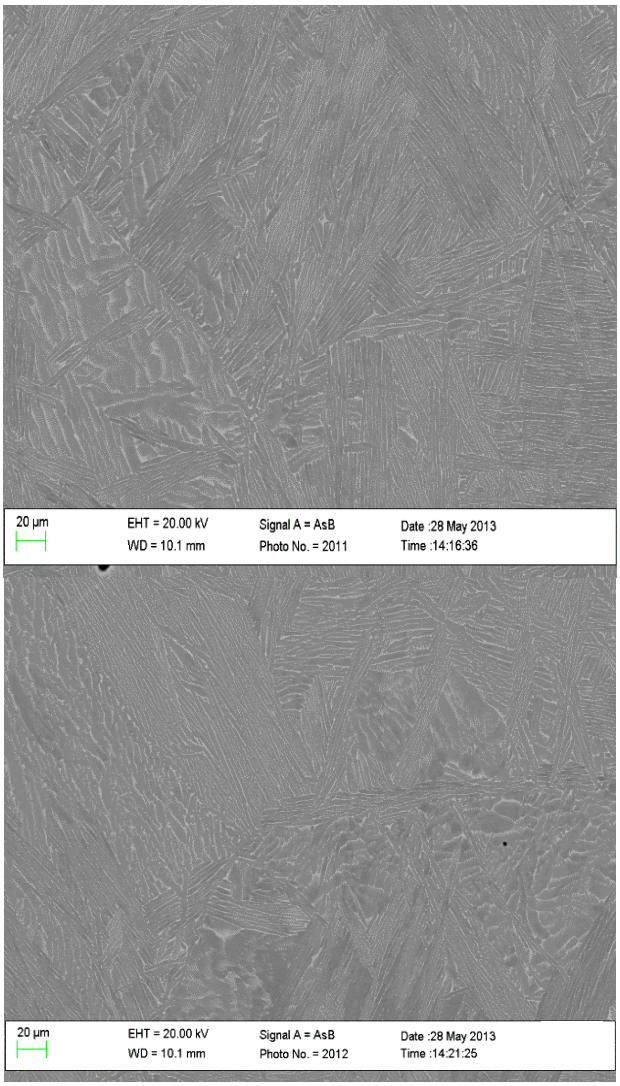

Figure 6. SEM microstructure image of machined Ti-6Al-4V alloy (Sample ID: 12)

REFERENCES

[1] Vinicius. A.R. Henriques, 2009 "Titanium production for aerospace applications," Journal of Aerospace and technology.

[2] Shunting Lei, Wenjie Liu, 2002, "High speed machining of titanium alloys using the driven rotary tool," International journal of machine tools and manufacture.

[3] Denis Noland, William Sebring, Yair Bruhis, 2001, "High performance milling in aerospace materials," Niagara cutters.

[4] Emsley, John, "Titanium- Nature's Building Blocks: An A-Z Guide to the Elements," Oxford, England, UK: Oxford University Press.

[5] C.H.Che-Haron, A.Jawaid, 2005, "The effect of machining on surface integrity of titanium alloy Ti-6Al-4V," Journal on materials processing technology.

[6] Lutjering, G.; Williams, J.C., 2003, "Titanium," Springer, Berlin.

[7] Donachie Jr. M. J., 1988, "Titanium: A Technical Guide," ASM International, Material Park, OH.

[8] Krebs, Robert E, 2006, "The History and Use of Our Earth's Chemical Elements: A Reference Guide (2nd edition)," Westport, CT: Greenwood Press.

[9] R.R. Boyer, 1996, "An overview on the use of titanium in aerospace industry," Journal on Material science and engineering.

[10] Donachie Jr., M. J., 1988, "Titanium: A Technical Guide," ASM International, Material Park, OH.

[11] Jiang Hua, Rajiv Shivpuri, 2004, "Prediction of chip morphology and segmentation during the machining of titanium alloys," Journal of Materials processing and Technology.

[12] Chinmaya R. Dandekar, John Barnes, Yung C. Shin, 2009, "Machinability improvement of titanium alloy (Ti-6Al-4V) via LAM and hybrid machining," International Journal of Machine Tools and Manufacture.

[13] Llorentz.J.I, Lopez de lacalle.L.N, Perez.J, Sanchez.J.A, 2000, "Advanced cutting conditions for the milling of aeronautical alloys," Journal of Materials processing Technology.

[14] Nouari, M., Ginting. A., 2006, "Wear characteristics and performance of multi-layer CVD-coated alloyed carbide tool in dry end milling of titanium alloy."

ASME District F - Early Career Technical Conference Proceedings
ASME District F - Early Career Technical Conference, ASME District F – ECTC 2013
November 2 – 3, 2013 - Birmingham, Alabama USA

POWDER-BED ELECTRON-BEAM-MELTING ADDITIVE MANUFACTURING: POWDER CHARACTERIZATION, PROCESS SIMULATION AND METROLOGY

Xibing Gong, Bo Cheng, Steven Price and Kevin Chou
Mechanical Engineering Department
The University of Alabama
Tuscaloosa, Alabama, USA

ABSTRACT

Among a broad spectrum of additive manufacturing (AM) technologies, powder-bed electron-beam-melting (PB-EBM) AM uses a high-power electron beam to melt and fuse metal or alloy powders to fabricate, layer-wise, a solid subject with geometry from electronic data. Metal AM greatly expands the capability of AM from rapid prototyping to direct digital manufacturing of functional engineering components. Different alloys such as Ti-6Al-4V have been widely studied for a variety of applications in aerospace, medical and automotive industries, etc. Despite unique advantages such as producing complex geometry designs and tooling-free production, there are still considerable challenges in metal AM, e.g., part accuracy and properties, as well quality consistency.

In a research project focused on the PB-EBM AM, several aspects critical to the process performance and part properties have been studied including powder characterizations, thermal modeling and process temperature measurements. Ti-6Al-4V powders from different conditions were studied by metallography and scanning electron microscopy. Finite element analysis (FEA) was applied to model the thermal phenomena for build part temperature simulations. Moreover, a near-infrared (NIR) thermal imager was employed to measure part surface temperatures during the build process. The results obtained so far indicate the following. (1) Metal powders have a much lower thermal conductivity compared to the solid counterpart because of porosity. (2) FEA simulation is capable of predicting build part temperatures and the melt pool sizes. (3) The developed NIR thermography is able to measure part surface temperatures, of high spatial resolution, around the electron beam scanning area during the build process.

INTRODUCTION

Additive manufacturing (AM) based on "layer-by-layer" fabrication is a group of technologies, by which physical solid parts are made directly from electronic data, generally files from computer-aided design (CAD) software. This group of technologies offers many design and manufacturing advantages such as short lead time, design freedom in geometry, and it is tooling free. Powder-bed electron-beam-melting (PB-EBM) is a relatively new AM technology [1]; it utilizes a high-energy electron beam, as a moving heat source, to melt and fuse metal powders and produce parts in a layer-building fashion. In building each layer, the processes involve powder spreading, pre-heating, as well as contour and hatch melting. In powder spreading, a metal rake is applied to uniformly distribute one layer of powders. Then, pre-heating is applied using a single beam at a high speed (15 m/s), with multi-pass scans, to reach a high temperature across the entire powder-bed surface. Following pre-heating, contour/hatch-melting stages take place, during which electron beams, either multiple split or single, move across the powder-layer surface tracing the model cross-section contour and then raster-scan through the inside of the contour at a lower scanning speed (e.g., 0.5 m/s). Once a build is completed, the system is cooled down and then the entire powder bed is retrieved from the machine for cleaning: sand blasting to clean off sintered powders from the build part. In post-processing, support structures, if any, will be removed, mostly by a mechanical means. PB-EBM is one of a few AM technologies capable of making full-density metallic parts, which drastically broadens AM applications in a wide variety of industries [1, 2].

Despite the advantages and potential benefits of PB-EBM AM, there exist several challenges for effective usage and widespread applications. In this paper, three technical aspects that have been studied from this PB-EBM AM research program are reported with methodology and current results discussed; they are powder characteristics (porosity and thermal conductivity), process thermal characteristics from the model, and from experiments, near infra-red thermography. The overall goal is to develop correlations between feedstock metal powder characteristics, thermal process modeling/metrology, and properties of PB-EBM AM parts for process and part quality control.

Different from laser-based metal AM processes, the EBM process applies the preheating to sinter the precursor powder layer by using electron beam at a low power and a high speed. According to the study by Cormier et al. [3] and Rodriguez et al. [4], the preheating serves with two purposes, holding the metal powders in place during subsequent melting and reducing the thermal gradient between the melted layer and the rest of the build part. The microstructure characterization of pre-heated sintered powders has been attempted in the current

study. Moreover, it is known that the thermal properties of metallic powders are significantly different from those of the corresponding solid bulk material [5, 6], especially, the thermal conductivity. Also, the thermal properties of metal powders are strongly temperature dependent. In addition, the EBM process operates at a high vacuum, and thus, the thermal conductivity of powders is not the same as in a gas surrounding [7]. Tolochko et al. [8] investigated the mechanisms of selective laser sintering of Ti powders and heat transfer in vacuum conditions. Accurate powder properties are desired to better simulate the thermal process. In the current research, the thermal conductivity of pre-heated Ti powders has been tested experimentally to support the thermal model.

Due to high energy intensity, complex heat transport modes and nonlinearity of the problem, simulations of the thermal phenomenon in EBM are an interesting, though challenging, research task. In general, the heat source, from electron beam interactions, is modeled as a conical volumetric heat flux underneath the workpiece surface [9-12]. The intensity is approximated as a Gaussian distribution horizontally and decays linearly with the depth [13, 14]. To account for radiation, Sih and Barlow [15] developed a porosity dependent model to predict the emissivity for different material conditions and environments, thus porosity dependent thermal properties can be applied. Zäh and Lutzmann [9] developed a simplified mathematical-physical model using an FEA method based on the general heat conduction equation and a mathematically abstracted heat source model. Melt pool geometry, as a function of various combinations of the beam scan speed and the beam power, was investigated. Shen and Chou [16] developed an FEA model, incorporating Gaussian heat flux distribution, fusion latent heat, and both porosity as well as temperature-dependent thermal properties, to simulate the transient heat transfer in the EBM. The FEA model was then used to evaluate the powder porosity effects on the temperature distributions and history. The simulated results showed a larger melt pool size with higher temperature in the powder layer than solid layer. With the increase of powder porosity, the melt pool temperature increased simultaneously. Chou [17] recently applied the developed FEA model [10] to explore the thermal characteristics during the EBM affected by different thermal properties. The results showed that the melting temperature could be the most dominant factor to the melt pool size for work materials of low conductivity, for materials of very high thermal conductivity such as copper, the role of the thermal conductivity may outweigh the melting point to strongly affect the melt pool size. In this research, different sets of process parameters in EBM were conducted to simulate the process parameters effects on the melt pool geometry.

The ability to measure the temperatures that occur during the EBM build process is an essential capability in order to verify process models, predict part microstructure, and develop feedback control systems. Thermocouples and several types of infrared cameras have been used to measure process temperatures in various types of AM processes. Because AM involves a fast, transient heat source, the limited spatial temperature resolution and slow response time of thermocouples limits their use when monitoring AM processes. Non-contact infrared (IR) imagers have been utilized in AM temperature measurement because of their excellent spatial temperature resolution and fast response time. Infrared cameras sensitive in the near-infrared (NIR) spectrum (0.8-2.5 μm) are better suited for measuring high temperatures (>1000 K), and also provide the benefit of being less sensitive to surface emissivity. Schwerdtfeger et al. (2012) [18] used a FLIR A320 infrared camera with a resolution of 320 × 240 pixels and a spatial resolution of 0.83 mm per pixel to detect flaws during an EBM process. The IR camera captured images of the powder bed surface after the completion of each layer being investigated. The captured IR images had low resolution; however, the general locations of flaws were detectable. Rodriguez et al. (2012) [4] used a FLIR SC635 infrared camera with a resolution of 640 × 480 pixels and a spatial resolution of 350 μm per pixel as part of a feedback control system for an Arcam A2 EBM system. They also captured images of the part after each layer of interest was completed. Non-uniform temperature distributions were easily identified with the IR camera. In the current research, an NIR camera has been employed to capture images of the EBM build process including the preheating, contour melting, and hatch melting portions of the layer fabrication process. The repeatability of the temperature measurements is studied as well as effects from build height.

TECHNICAL STUDIES

Powder Characterization

The raw material used was Ti-6Al-4V powders. A simple CAD model was designed (hollow disk) to preserve powders from preheating, as can be seen from Figure 1. The preheat temperature was about 730 °C, and the process lasted for about 5 s. After the preheating process, the samples were sectioned and mounted with epoxy. Fine polishing was applied, and an optical microscope (OM) and a scanning electron microscope (SEM) were used to observe the microstructures of the powders. Etching was applied using the Kroll's Reagent in order to reveal the phase information of the preheated powders.

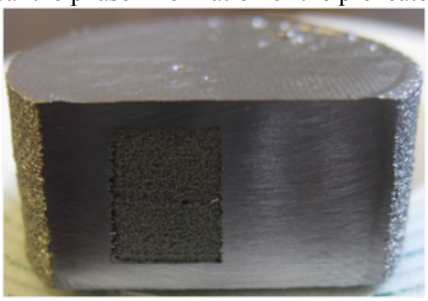

Figure 1. Illustration of the Sample Containing Powders from Preheating

For the raw material, fine powders, with a diameter normally between 45 and 100 μm, were used. Figure 2 shows

the SEM image of Ti-6Al-4V raw powders: particle distributions (Figure 2(a)) and a single powder (Figure 2(b)). Small satellite powders are located around larger powders. During each layer build, a layer of powders is formed first, followed by preheating for powder sintering, prior to each layer deposition. A typical layer thickness is in the range of 0.07 to 0.15 mm.

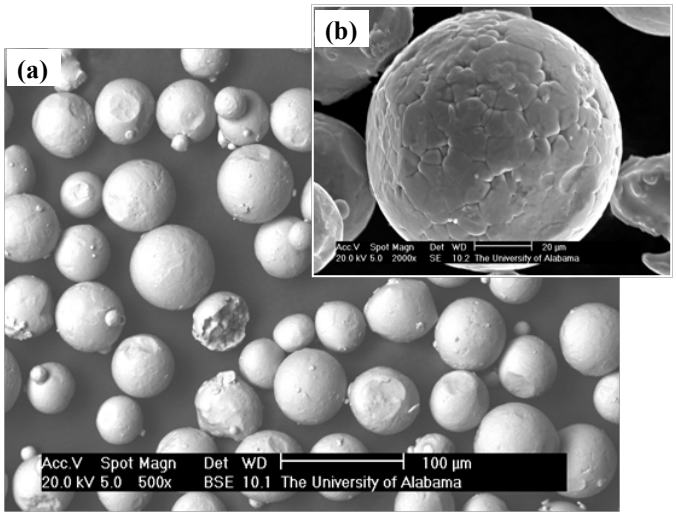

Figure 2. SEM Images of Ti-6Al-4V Powders: (a) Particles with Different Sizes and (b) an Individual Particle

After preheating, a certain extent of inter-particle cohesion or aggregation is expected to be formed. Figure 3 shows SEM images of the aggregated powders of the powder-bed sample. The necks could be seen clearly at the build surface. The diameter of the necks is on the order of 1 µm to 10 µm. The metallurgical connection or partial melt is expected to occur during the preheating process. The morphology of the powder-enclosed sample is shown, after metallographic preparations, in Figure 4. The necks are shown between some powders, although pulling-out of some powders happened due to mechanical polishing. He et al. [19] did the research on the microstructure of the EBM Ti-6Al-4V powders. The authors found that the powders satellite particles in interspace are connected to large spherical particles, consistent to observations from this study.

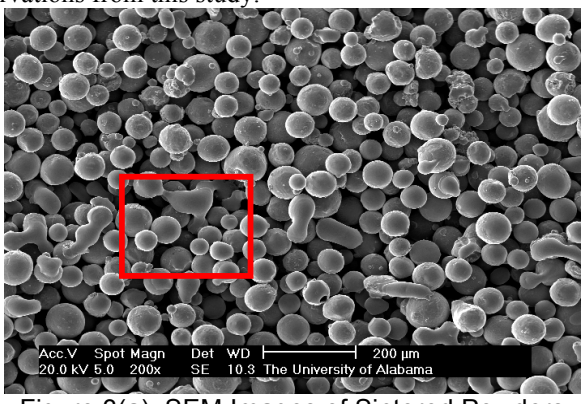

Figure 3(a). SEM Images of Sintered Powders

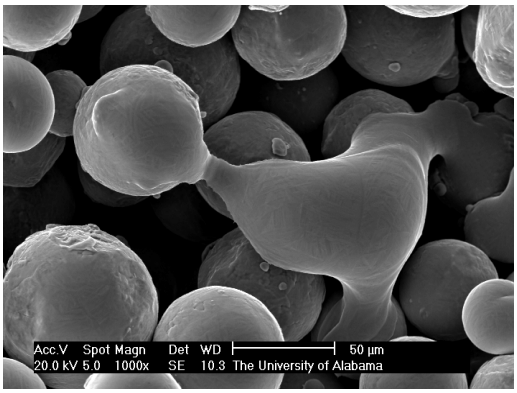

Figure 3 (b). SEM Images of Sintered Powders (inset)

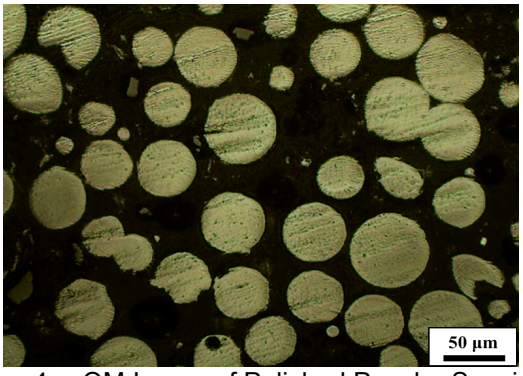

Figure 4. OM Image of Polished Powder Specimen

After etching, the phases in the alloyed powders are revealed. Generally, the microstructure has a basketweave morphology and intergranular structures, as seen in Figure 5, which are comparable to the microstructure of solid Ti-6Al-4V [20]. Ti-6Al-4V is an $\alpha+\beta$ alloy and its microstructure is strongly dependent on its thermal history. The primary phase is body-centered cubic β. When the β-transus temperature is reached, the transformation into the hexagonal closed-packed α phase begins [21]. In the microstructure (Figure 5), the light region is α phase, and the dark area corresponds to the β. For the raw powders, the primary phase is the bulk α phase.

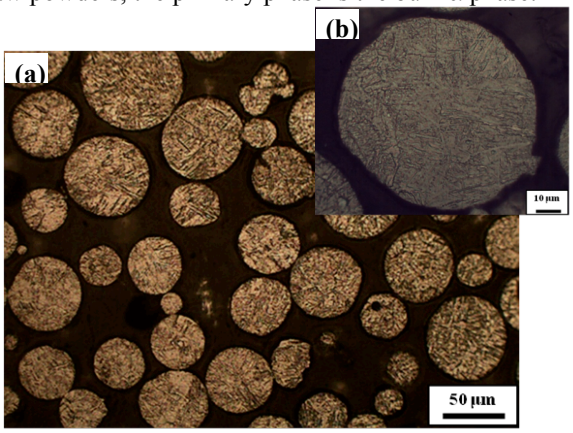

Figure 5. OM Images of Powder Sample after Etching: (a) Powder Population and (b) Single Powder

In addition, an approach has been attempted to investigate the thermal properties of powders, as in the powder-bed condition, using a thermal analyzer. Specimens of hollow block (40 mm by 40 mm by 13 mm with 2.54 mm shell thickness) were designed using CAD software and further fabricated using an EBM system (S12 from Arcam) with Ti-6Al-4V powders and default process parameters (70 um layer thickness), with 13 mm dimension along the Z direction (build direction). A solid piece of the same overall dimensions was fabricated as well to evaluate the thermal conductivity of solid Ti-6Al-4V.

The hollow and solid specimens were measured with thermal properties at different temperatures (up to 750 °C), using a T2500S thermal analyzer by Thermtest. The results are summarized in Figure 6 below. It is first noticed that the thermal conductivity of solid Ti-6Al-4V is about 6.2 W/m·K at room temperature, which is close to literature data. The thermal conductivity is also found isotropic for the solid piece. With increased temperatures, thermal conductivity values increase, to around 10 W/m·K, at 750 °C, which is not as high as reported in literature (~15 W/m·K). For the powder-contained specimen, the overall bulk thermal conductivity can be measured. With the thickness of powder and solid portions and the thermal conductivity of solid, the true powder thermal conductivity can be analyzed using the "series of heat conductance" method.

The results, also shown in Figure 6, demonstrate that metal powders have substantially lower thermal conductivity, about 2.7 W/m·K at room temperature and less than 4.0 W/m·K at 750 °C. Multiple measurements were acquired and the results are very repeatable, e.g., 2.1% standard deviation at 750 °C for the solid piece. The results support the hypothesis that thermal conductivity is very sensitive to the powder geometry characteristics, most likely porosity. For this testing, the calculated porosity is about 50%, based on the density ratio between the powder portion and solid.

Since the powder-containing specimen has a solid shell around the circumference, the heat loss toward the radial direction may affect the measured effective thermal conductivity along the build direction in calculating the true powder thermal conductivity. Moreover, the sintering effect is expected anisotropic too, and thus, it is interesting to evaluate thermal properties along the build direction (major heat dissipation direction). Additional testing was conducted to insulate the circumferential areas to minimize lateral heat flow, and approximate the unidirectional heat conduction. The measurements gave a true powder thermal conductivity, along the build direction, of 0.63 W/m·K at the room temperature and 2.44 W/m·K at 750 °C, about 25% of solid Ti-6Al-4V. This initial study unambiguously proves that metal powders will have significantly lower thermal properties, primarily thermal conductivity, that drastically affects the thermal behavior during electron scan melting. Moreover, the proposed method is able to obtain the thermal properties of materials as in the powder-bed packing condition, which is important in improving the model prediction capability.

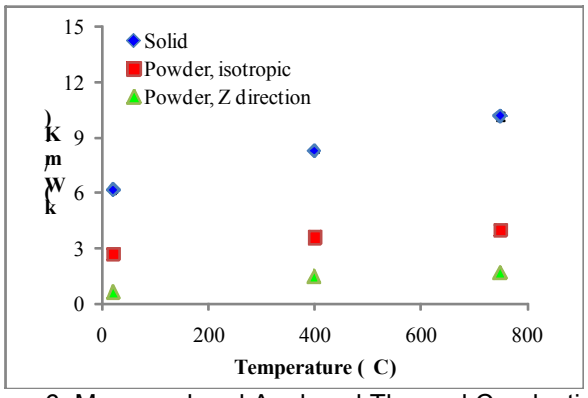

Figure 6. Measured and Analyzed Thermal Conductivity of Ti-6Al-4V Specimens: Solid and Powders

Process Simulations

A three-dimensional (3D) FEA thermal model was developed and implemented in ABAQUS 6.11, to comprehensively study the thermal process of EBM. Figure 7 below shows the simplified simulation domain illustrating the process and model. On top of the substrate a thin powder layer has been modeled and been considered as the latest added powder layer, the substrate base material is considered as the solid materials since it has been deposited in this model. The electron beam heating, simulated as a moving conical body heat source with Gaussian distribution horizontally and decaying linearly, starts at the top powder layer surface and scans along the *x*-direction with a given constant speed. Since the EBM process is in vacuum environment, the convection between the workpiece and environment is not considered, only the thermal radiation is considered in the heat transfer mode between the model and surroundings.

A user subroutine of DFLUX, which can read simulation time step and model coordinates, is used to determine the domain of the volumetric heat flux. To provide a better understanding of the EBM thermal process, temperature-dependent material properties have been considered in the simulation. The detailed modeling set up and material property information can be found in [16]. A uniform temperature distribution of $T_{preheat}$ has been assigned to the solid substrate and top powder layer as the thermal initial condition.

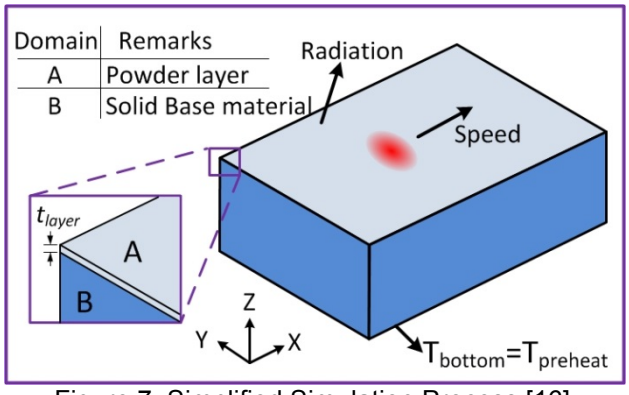

Figure 7. Simplified Simulation Process [16]

The thermal model was then applied to evaluate the effects of process parameters (beam speed (V), beam power (P) and beam diameter (D)) on the melt pool geometry for the case of Ti-6Al-4V in EBM. Other process parameters, such as layer thickness, powder porosity, and preheat temperature, etc., are listed in Table 1.

Table 1. Process Parameters Used in Simulation [16]

Parameters	Value
Absorption efficiency, η	0.9
Powder layer thickness, T_{layer} (mm)	0.1
Porosity, φ	0.45
Beam penetration depth, Pd (mm)	0.1
Preheat temperature, $T_{preheat}$ (°C)	730

For each simulated result, the thermal transient temperature distribution phenomenon can be considered as a quasi-steady state if the scanning path is long enough. Then, the Ti-6Al-4V liquidus temperature is used to define melt pool boundary. Based on the liquidus-boundary, the melt pool geometry (length, depth, and width) can be obtained. Figure 8 shows a schematic diagram representing a melt pool geometry. It is generally a 3D cross-sectional view (cutting through the electron beam scanning centerline), with temperature legends adjusted to highlight the melt pool boundary. The melt pool length, width and depth are strongly affected by process parameters. Figure 9 lists several simulated cases under different combinations of process parameters for their effects on the melt pool sizes.

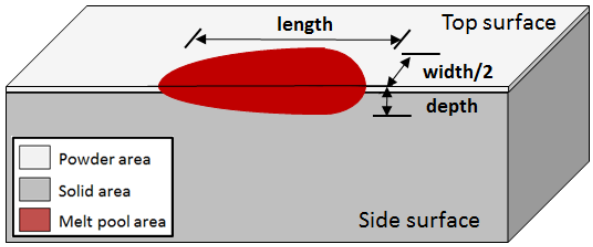

Figure 8. Schematic Diagram of Melt Pool Geometry

From the heat input consideration, it is intuitive that a higher beam power will increase the temperatures and the melt pool size since more energy is absorbed into the part. To show the effects of the beam power, three beam power values, from 120 W to 360 W, have been tested with the same beam speed and diameter. The results from Figure 9(a) demonstrate that the melt pool dimensions (length, depth and width) generally increase with the increase of the beam power. The maximum temperature also increases at the same time.

A reduced maximum temperature and heat penetration can be expected with the increase of the beam diameter due to the decrease of the beam energy density. The effect of the beam diameter could be seen from Figure 9(b). It presents that the melt pool size increases in width but decreases in depth and length with the increase of the beam diameter. The maximum temperature also decreases with the increased beam diameter.

Since a faster scanning velocity may cause a lower beam energy density per unit time, a lower temperature distribution along the scanning path will be anticipated. Figure 9(c) shows that, the temperature decreased with the increase of beam velocity; meanwhile, the melt pool size becomes smaller in all dimensions.

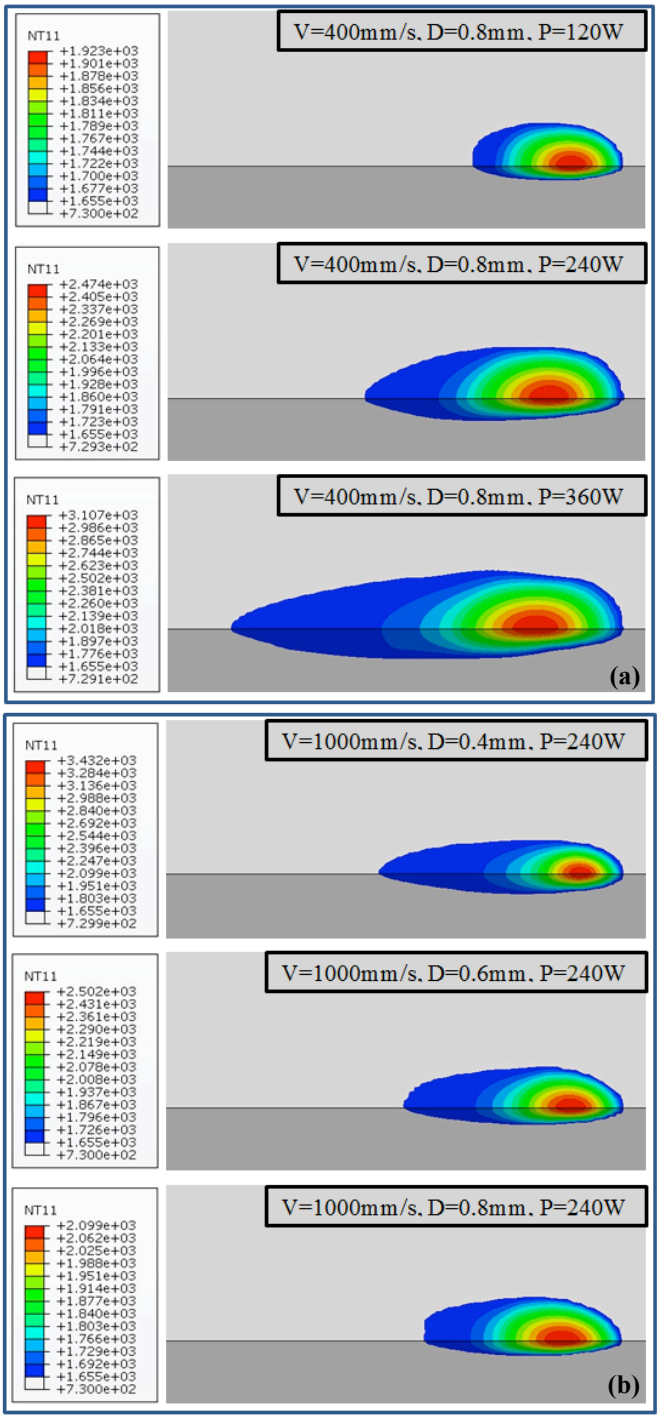

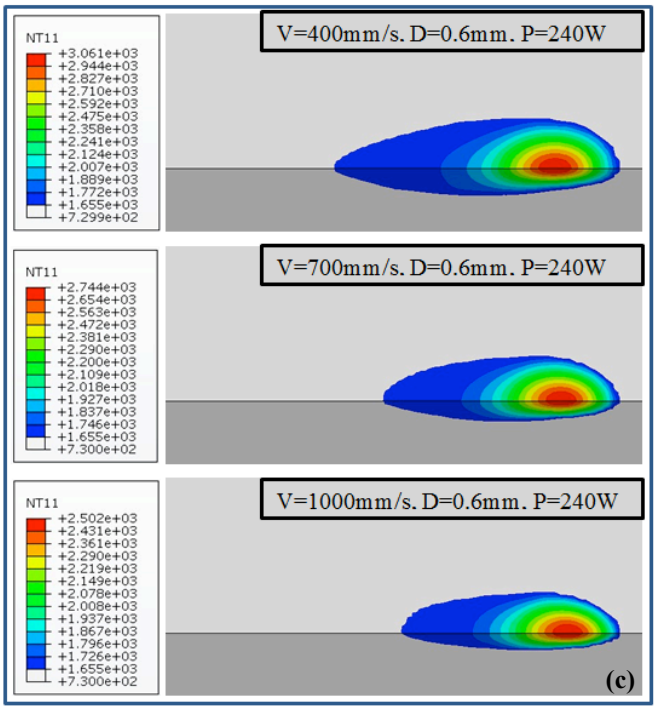

Figure 9. Simulation Results Comparisons: (a) Beam Power Effect, (b) Beam Diameter Effect, and (c) Beam Speed Effect

Process Metrology

An Arcam S12 EBM machine at NASA's Marshall Space Flight Center was used to build the test parts. Temperature measurements of the EBM process were made with a LumaSense MCS640 NIR infrared camera. The NIR camera has a spectral range of 0.78-1.08 µm and a 640 x 480 pixel uncooled focal plane array (FPA) sensor. The image capturing system has a maximum frame rate of 60 Hz and a detectable temperature range of 735-2446 °C which is divided into three temperature ranges: low (735-1108 °C), medium (1057-1485 °C), and high (1503-2446 °C). The camera has a lens with a minimal 500 mm working distance and a view area of 31 mm x 23 mm at 500 mm distance. The camera was calibrated with the glass in the viewport of the EBM machine so that a transmission rate of unity will correctly account for the transmission losses due to the glass. The powder material used was Ti-6Al-4V. The emissivity of the surface is unknown so measurements were taken with assumed emissivities of 0.35 and 0.5. The integration time of the image capturing system is 16.25 ms, 1.7 ms, and 50 µs for the low, medium, and high temperature ranges respectively. The data acquisition system consists of a laptop and an Ethernet cable, connected with a gigabit Ethernet express card.

The NIR camera is mounted on a tripod and positioned to look downward through the EBM machine's viewport onto the build platform. The camera is vertically inclined at 35° from the surface normal with minimal roll angle and horizontal yaw. More detail on the experimental setup may be found in Price et al. (2012) [22]. The EBM machine contains a heat shield that is placed between the viewport and the build platform. This heat shield has a cutout for viewing the build platform but that cutout is obstructed with vertical bars. Three of these bars were cut to provide a clear view of the build platform, but interference from a single bar was still observed during testing.

The different temperature ranges of the NIR camera are each uniquely suited for imaging the various stages of the fabrication process. The low temperature range is best suited for preheating, the medium temperature range for contour melting, and the high temperature range for hatch melting. Examples of NIR images of the various portions of the EBM process are shown in Figure 10. The images are from the fabrication of a 30.48 mm × 25.4 mm solid cross section. The spatial resolution of the NIR images is determined by identifying the edges of the part during the contour melting phase, then determining the number of pixels between these edges. The average horizontal and vertical spatial resolutions of the images are found to be 46.8 µm/pixel and 66.2 µm/pixel respectively. The vertical spatial resolution is larger due to distortion caused by the 35° tilt of the camera.

A two-dimensional (2D) temperature profile along the scan path during hatch melting is generated for each hatch melting frame. The profiles were aligned with each other and averaged for each build layer whose fabrication is recorded. An example of one of these average temperature profiles is shown in Figure 11.

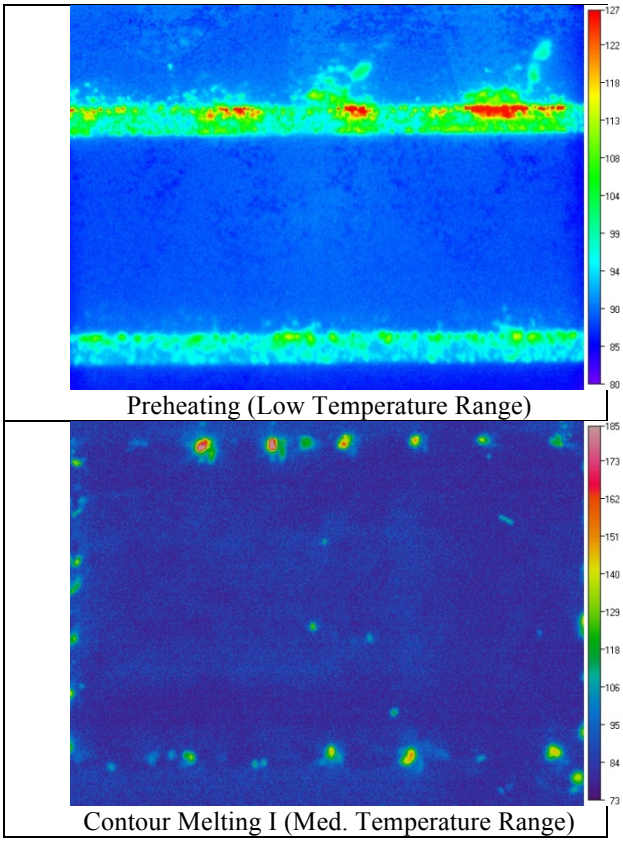

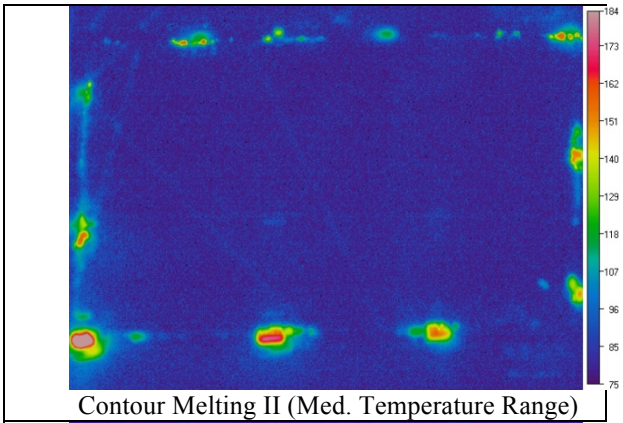

Figure 10. NIR Images of the Various Stages of the EBM Fabrication Process

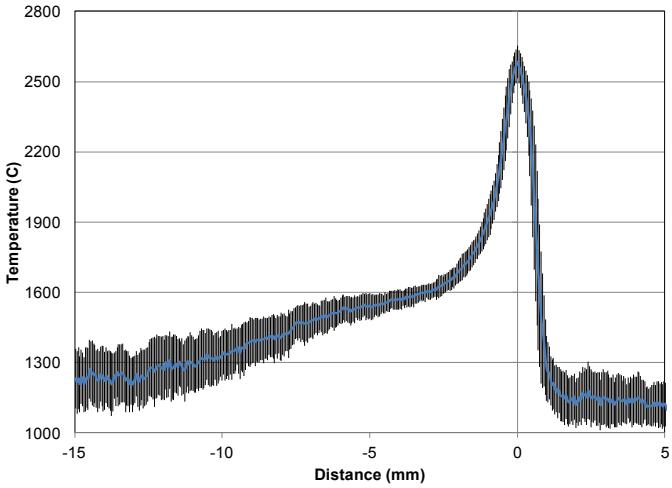

Figure 11. Temperature Profile of Hatch Melting

These average profiles are compared at various build heights as shown in Figure 12. The main build effect seen is the increased cooling rate at higher build heights. The horizontal distance between the solidus temperature and the peak temperature decreases with the build height.

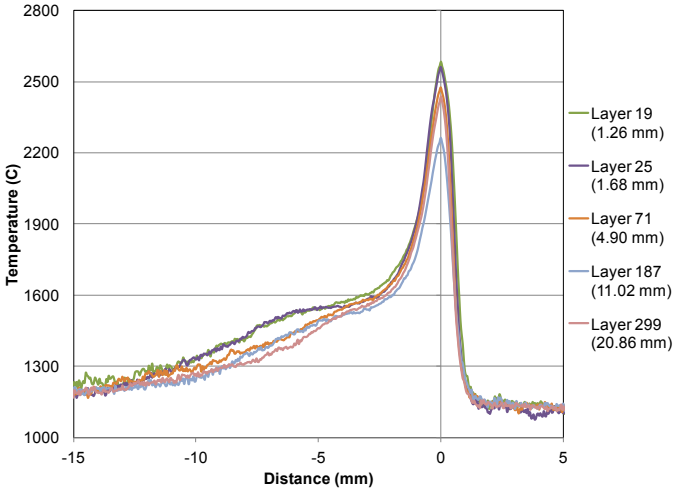

Figure 12. Average Temperature Profiles at Various Build Heights

CONCLUSION

In this study, Ti-6Al-4V powders used in EBM, in a sintered state, have been characterized. The thermal conductivity of sintered powders has also been analyzed. In addition, a developed 3D thermal model was applied to investigate process parameter effects on the part temperatures and the melt-pool sizes. Moreover, a near infra-red thermal imager was utilized to develop thermography for process temperature measurements. Some primary findings are listed below.

(1) The calculated porosity for the powders is about 50%. The metal powders have significantly lower thermal conductivity than that of solid. It may drastically affect the thermal behavior during electron scan melting. Also, the thermal conductivity is highly temperature dependent for the powders: about 0.63 W/m·K at room temperature and less than 2.44 W/m·K at 750 °C.

(2) A higher beam power will increase the maximum temperature and the melt pool size. However, the increase of the beam diameter or scanning speed results in a reduced maximum temperature and heat penetration. With the increase of the beam speed, the melt pool size becomes smaller in all dimensions. On the other hand, the melt pool size increases in width, but decreases in depth and length with the increase of the beam diameter.

(3) The part surface temperature during the EBM process has been successfully measured with high spatial resolution using the NIR thermography. The different temperature ranges of the NIR camera are suited for imaging the various stages (preheating, contour and hatch melting) of the EBM fabrication process. Analyzed 2D temperature profiles along the beam path, at the beam center, show results as a moving heat source condition, with a plateau region corresponding to the liquidus-solidus temperatures.

Future studies will be focused on integrating the powder thermal characteristics, thermal simulations and NIR

temperature measurements to develop process parameter envelop for effective usage of the PB-EBM technology.

ACKNOWLEDGEMENTS

The materials presented in this paper are supported by NASA, under award No. NNX11AM11A. The research is in collaboration with the Marshall Space Flight Center, Advanced Manufacturing Team. Assistance from and discussions with Majid Babai, Kenneth Cooper and James Lydon are greatly appreciated.

REFERENCES

[1] Gong, X., Anderson T., and Chou K., 2012, "Review on Powder-based Electron Beam Additive Manufacturing Technology," Proceedings of ASME 2012 International Symposium on Flexible Automation (ISFA), St. Louis, MO, June 18-21, 2012, ISFA2012-7256.

[2] Biamino, S., Penna, A., Ackelid, U., Sabbadini, S., Tassa, O., Fino, P., Pavese, M., Gennaro, P., and Badini, C., 2010, "Electron beam melting of Ti-48Al-2Cr-2Nb alloy: Microstructure and mechanical properties investigation," Intermetallics, 19(6), pp. 776-781.

[3] Cormier, D., Harrysson, O., and West, H., 2004, "Characterization of H13 steel produced via electron beam melting," Rapid Prototyping Journal, 10(1), pp. 35-41.

[4] Rodriguez, E., Medina, F., Espalin, D., Terrazas, C., Muse, D., Henry, C., MacDonald, E., and Wicker, R., 2012, "Integration of a Thermal Imaging Feedback Control System in Electron Beam Melting," WM Keck Center for 3D Innovation, University of Texas at El Paso, pp. 945-961.

[5] Lin, T. H., Watson, J. S., and Fisher, P. W., 1985, "Thermal conductivity of iron-titanium powders," Journal of Chemical & Engineering Data, 30(4), pp. 369-372.

[6] Sih, S. S., and Barlow, J. W., 2004, "The prediction of the emissivity and thermal conductivity of powder beds," Particulate Science and Technology, 22, pp. 291-304.

[7] Roberts, I. A., Wang, C. J., Esterlein, R., Stanford, M., and Mynors, D. J., 2009, "A three-dimensional finite element analysis of the temperature field during laser melting of metal powders in additive layer manufacturing," International Journal of Machine Tools and Manufacture, 49(12-13), pp. 916-923.

[8] Tolochko, N. K., Arshinov, M. K., Gusarov, A. V., Titov, V. I., Laoui, T., and Froyen, L., 2003, "Mechanisms of selective laser sintering and heat transfer in Ti powder," Rapid Prototyping Journal, 9, pp. 314-326.

[9] Zäh, M. F., and Lutzmann, S., 2010, "Modelling and Simulation of Electron Beam Melting," Production Engineering, 4(1), pp. 15-23.

[10] Liu, C., Wu, B., and Zhang, J., 2010, "Numerical Investigation of Residual Stress in Thick Titanium Alloy Plate Joined with Electron Beam Welding," Metallurgical and Materials Transactions B, 41(5), pp. 1129-1138.

[11] Luo, Y., Liu, J., and Ye, H., 2010, "An analytical model and tomographic calculation of vacuum electron beam welding heat source," Vacuum, 84(6), pp. 857-863.

[12] Rouquette, S., Guo, J., and Le Masson, P., 2007, "Estimation of the parameters of a Gaussian heat source by the Levenberg-Marquardt method: Application to the electron beam welding," International Journal of Thermal Sciences, 46(2), pp. 128-138.

[13] Lankalapalli, K., Tu, J. F., and Gartner, M., 1996, "A model for estimating penetration depth of laser welding processes," Journal of Physics D: Applied Physics, 29, pp. 1831.

[14] Tsirkas, S. A., Papanikos, P., and Kermanidis, T., 2003, "Numerical simulation of the laser welding process in butt-joint specimens," Journal of Materials Processing Technology, 134(1), pp. 59-69.

[15] Sih, S. S., and Barlow, J. W., 2004, "The prediction of the emissivity and thermal conductivity of powder beds," Particulate Science and Technology, 22, pp. 291-304.

[16] Shen, N., and Chou, K., 2012, "Thermal Modeling of Electron Beam Additive Manufacturing Process-Powder Sintering Effect," Proceedings of ASME 2012 International Manufacturing Science and Engineering Conference (MSEC), MSEC2012-7253, Notre Dame, IN, June 4-8, 2012.

[17] Chou, K., 2013, "Numerical Evaluations of Thermal Property Effects in Electron Beam Additive Manufacturing," Proceedings of NAMRI/SME, (41), NAMRC41-1551, Madison, WI, June 10-14, 2013.

[18] Schwerdtfeger, J., Singer, R. F., and Körner, C., 2012, "In situ flaw detection by IR-imaging during electron beam melting," Rapid Prototyping Journal, 18(4), pp. 259-263.

[19] He, W., Jia, W., Liu, H., Tang, H., Kang, X., and Huang, Y., 2011, "Research on preheating of Titanium alloy powder in electron beam," Rare Metal Materials and Engineering, 40(12), pp. 2072-2075.

[20] Al-Bermani, S.S., Blackmore, M.L., Zhang, W., and Todd, I., 2010, "The origin of microstructural diversity, texture, and mechanical properties in electron beam melted Ti-6Al-4V," Metallurgical and Materials Transactions A, 41A, pp. 3422-3434.

[21] Eschey, C., Lutzmann, S., and Zaeh, M.F., 2009, "Examination of the powder spreading effect in Electron Beam Melting (EBM)," Solid Freeform Fabrication, Austin, TX, August 3-5, pp. 308-319.

[22] Price, S., Cooper, K., and Chou, K., (2012), "Evaluations of Temperature Measurements by Near-infrared Thermography in Powder-based Electron-beam Additive Manufacturing," 23rd Annual International Solid Freeform Fabrication Symposium, Austin, TX, Aug. 6-8, 2012.

ASME District F - Early Career Technical Conference Proceedings
ASME District F - Early Career Technical Conference, ASME District F – ECTC 2013
November 2 – 3, 2013 - Birmingham, Alabama USA

ORIGIN OF MATERIALS: WHERE OUR METALS COME FROM AND WHY THE ENGINEERING WORLD CARES.

Matthew L. Schulte
Burns & McDonnell
Kansas City, Missouri, United States of America

ABSTRACT

There is no denying over that the last 25 years globalization has spread to more industries than ever before. One of the industries most affected has been steel production. While in years past, much of United States construction steel came from the US, Western Europe, or Japan, this is not the case today. Many new countries such as China, South Korea, and India have entered the global steel market, and are eating into the market share formerly held by the regions listed above. Globalization has served to keep the price of steel in check; however, concerns with regards to quality have been raised. Past incidents have proven that not all steel is fabricated to the specification it claims to be. So the question becomes, how can engineers ensure materials are up to specification?

Nowhere are these quality concerns more apparent than in process industries, such as oil refining and gas production. Safety and operability concerns lead these companies to become incredibly sensitive to material quality. Past accidents have proven that ensuring the material ordered is in compliance with its specification is of the utmost importance.

So how can engineers verify that material properties match what was ordered? The first step in this process is to know how these materials are manufactured and tested. The second step is to take additional action when a fear of incorrect material properties is present, such as testing by an independent party to confirm vendor results. Utilizing trusted quality assurance procedures also helps to verify a consistent, quality product. Taking these steps can reduce material quality concerns. Once this due diligence is performed, the purchaser may utilize low cost labor source countries effectively, without sacrificing quality of safety of the final product.

INTRODUCTION

Globalization is changing the way the world economy works. Materials are no longer bought locally. Purchases can now be done over the phone or internet, around the world, without ever setting foot in the product's manufacturing plant. The construction industry has changed in light of this globalization. With this change, new challenges and opportunities have arisen. One of the most prominent challenges that has arisen due to globalization of manufacturing is that of counterfeit or substandard materials. This has caused the process industry particular strife, since a failure in construction material is nearly always unacceptable and can lead to serious safety and economic consequences. This is especially true in boiler, pressure vessel, and pipe fabrication. While this paper focuses on all substandard and counterfeit materials, the conclusions and recommendations drawn are targeted for purchasers and end users of vessel-grade steel plate and forgings.

GLOBALIZATION

Due to the changing economic climate from increased globalization, the world economy has drastically changed. Between 1980 and 2011 the World Trade Organization estimated that global exports of total merchandise increased from $2.03 trillion to $18.29 trillion (in current prices) [1]. Globalization has had a major impact on many industries, including that of steel production. Over this same time period, global steel exportation grew from a $77 billion to a $527 billion market. In the same 31 years, the exported total value of steel from China alone grew $55.23 billion. Steel exports from India and Brazil increased by $13.25 billion and $11.66 billion, respectively. Over this time, US steel imports increased from an $8.15 billion market in 1980 to a $40.94 billion market in 2011. In 1980, the largest steel exporting country in the world was Japan. Germany and France were second and third, respectively, with the US ranking sixth. China was not even in the top 10. By 2011, China was the largest exporter, outpacing second ranked Japan by 19% and well past the US at tenth [2].

As previously noted, the largest amounts of growth have come from countries that organizations, such as the International Monetary Fund, would label as developing economies. Developing economies now produce a majority of the world's steel. Developed economies represent only 3 of the top 10 steel producing countries. These figures are shown in Table 1.

This globalization has served to keep the price of steel in check. Rising prices of steel from traditional exporting countries like the United States or Japan have led purchasers to consider new manufacturers. The change in origin of materials

has brought new challenges for manufacturers and purchasers alike. Purchases are now made around the world, not from across the country which has made it more difficult for quality auditing to be performed. If purchasers are not careful, they can buy materials from an inferior, or worse, unscrupulous manufacturer. Purchasing of materials then becomes similar to purchasing a car without a test drive, or purchasing a house without a walkthrough. To resolve some of these challenges, thorough supplier quality procedures have been developed.

Table 1. Steel production of developing and developed economies, 2012 [13]

Largest Steel Producing Countries, Developed Economies		
Country	2012 Total, in thousand metric tons	World Rank
Japan	107,234.68	2
United States	88,598.34	3
Germany	42,661.26	7

Largest Steel Producing Countries, Developing Economies		
Country	2012 Total, in thousand metric tons	World Rank
China	708,784.00	1
India	76,715.00	4
Russia	70,607.90	5
South Korea	69,320.59	6
Turkey	35,884.51	8
Brazil	34,682.00	9
Ukraine	32,910.75	10

The great fear for a purchaser is whether or not material purchased truly conforms to the specified standard. Materials that do not meet the specified standard are classified as either counterfeit or substandard.

COUNTERFEITS AND SUBSTANDARD MATERIAL

As globalization has risen, so has counterfeiting. Little research into why the overall quantities of counterfeit materials rose as globalization did has been completed; however, one can make the inference that since globalization rose predominately as a means to reduce production costs, counterfeiting became the ultimate cost reducer, as licensing fees, third party certifications, or expensive elements of production have been omitted altogether. Laypeople may consider counterfeiting simply to be an issue for clothing and consumer electronics manufacturers; however, the construction industry has not been immune to this practice. Senator Orrin G Hatch (R-Utah), stated in a 1995 press conference, “Perhaps most troubling is the widespread threat counterfeiting poses to public health and safety. Few Americans truly appreciate the significance, scope, or consequences for this crime” [3]. Past events have proven unscrupulous manufacturers will deliberately use counterfeit materials as a method of reducing productions costs, as evidenced by the examples below.

In 2004, Ralph Michael Cooper was sentenced to two-and-a half years in prison for selling counterfeit helicopter parts to the U.S. military [4]. Cooper was awarded a defense contract in which he was to provide seals for Black Hawk and Sea Hawk helicopters. Instead of being purchased from the military’s approved manufacturer, Cooper deliberately sourced the parts from a Taiwanese company, and sold the parts to the military at 20 times his cost.

In the 1990’s, the FAA estimated that 2% of the 26 million parts installed annually on airplanes were counterfeit. The parts were either considered to be made of substandard materials, made using forged documentation, or both. In 1991, a United Airlines mechanic discovered bearing-seal spacers for Pratt & Whitney jet engines that were counterfeit. The parts dealer, Gary Shafer, who pled guilty to trafficking counterfeit goods, had used phony OEM boxes and labels when selling parts [5].

22,848 seizures of merchandise were made by the US Customs in 2012. The total estimated value of these seizures was $1.26 billion. China was identified to be the largest source country, accounting for 72% of the seized goods. Hong Kong was second with a total of 12% of seized goods [6].

Counterfeit materials can be separated into three classes. First, manufacturers use the marking and design of a legitimate company or standard. Purchasers assume they are getting a known commodity, but the products typically lack the quality the purchaser expects. Second, parts are made to appear new. Third, material simply does not meet the requirements of its stated specification. The third class is also defined as substandard material.

At first glance, these items would seem to be unrelated, other than each presents the end user with a higher propensity towards failure. A problem with materials, especially forging and plate materials, is that they are often branded in a different way than other items, such as consumer electronics. One may be able to review by visual inspection the difference between a genuine and counterfeit OEM phone or clothing items, but the same review is often inconclusive when regarding pressure vessel plate. Some organizations do not differentiate language between counterfeit or substandard materials. The FAA, for instance, calls parts unapproved when they lack proper paperwork, rather than identifying true counterfeits versus genuine parts that simply have missing paperwork from the manufacturing process [5].

If the materials received are counterfeit or substandard, the recourse is still the same for a pressure vessel end user. Actions must be taken to confirm the safety and reliability of equipment. To minimize both cost and schedule impacts, the course of action is to perform extra non-destructive examination (NDE). The worst-case scenario (financially and schedule-wise) would be that of a total replacement. Between these two extremes, extra samples could be generated for in addition to NDE, and destructive testing could be used to

confirm material properties. However, extra material is not always available to generate a sample from the same material heat. Because the recourse for counterfeit or substandard materials is the same, often times the end user is unable to determine the root cause. An end user in the process industry is generally too concerned with trying to get a plant up and running, not using valuable time performing a full investigation to determine if materials are substandard or counterfeit. This investigation for this study found little evidence to show what investigatory practices are used by end users to determine if materials are indeed counterfeit or substandard.

With regards to steel, some manufacturers view producing substandard or counterfeit grade materials as an initial step towards becoming a legitimate supplier. Consider the Japanese manufacturing industry, which after World War II was considered to be inferior. Over time, Japan developed from a low-cost manufacturing region into one of the world's highest quality manufacturing sources. Interviews have shown that some manufacturers view this Japanese model as a legitimate business plan [7]. This is obviously a practice that cannot be condoned, as deliberately producing inferior steel puts end users safety in jeopardy.

The largest source country of counterfeit goods in the world is China. There are many reasons for continued counterfeiting in China, including the troubling practice of local government support or condoning of the counterfeiting practice [8]. The national government of Beijing creates laws and regulations that appear a sincere effort to stem the counterfeiting of goods; however, in some local economies within China, counterfeiting is such a large portion of the local economy that strictly enforcing counterfeiting laws would severely impact unemployment levels. Because of this, local municipalities are found to provide ineffective law enforcement regarding counterfeiting and can even defend counterfeiting stridently [8].

Being aware of counterfeiting that exists in the manufacturing industry helps the purchaser better understand how to reduce counterfeiting risk. Knowing in what instances counterfeiting is more likely to occur leads the purchaser to avoid these situations or provide more oversight of the manufacturing process. This additional oversight reduces the risk of a manufacturer counterfeiting materials, and thus reduces the risk of failure-prone materials ending up on a jobsite.

MATERIAL MANUFACTURING PROCESES

In order to understand where counterfeit and substandard materials come from, a purchaser must first understand how materials are made. The target audience of this study is purchasers and end users of vessel-grade steel plate and forgings. Thus, the manufacturing processes and material standards considered will focus on these materials.

Figure 1 shows a sample plate manufacturing process with material arriving as a slab or as a raw bulk quantity. Once the final products are formed, mechanical and chemical testing is performed to confirm the properties of the materials. This documented testing is the basis on which buyers and end-users ensure the materials received are as specified.

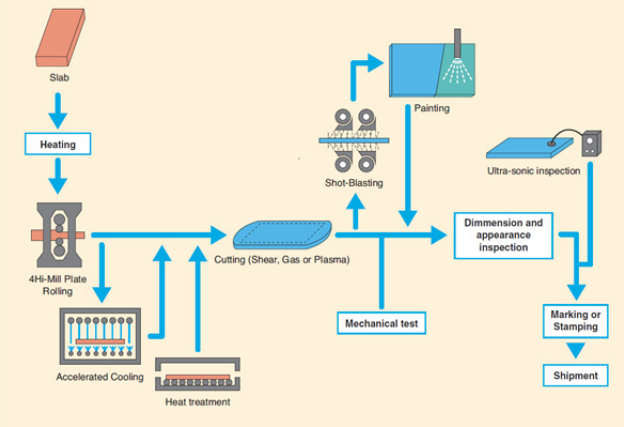

Figure 1. Sample Plate Manufacturing Process [14]

While Figure 1 shows part of a forging process, it does not show the complete sourcing process. The manufacturer who forms this forging needs to start with raw material. The raw material may be sourced from within the same company or an outside producer, which is where questions form regarding the true meaning of origin of materials. The mechanical and chemical tests for the final product are done after the final plastic deformation is performed [9]. Samples must be subject to the same plastic deformations as the finished product, per ASME and ASTM specifications [9].

Is the origin the point where the original metal is melted, or is it where the final manufacturing steps are done? Why do some purchasers specify melted and manufactured in approved regions, as opposed to manufactured and tested? By specifying that raw material is sourced from an approved region, the purchaser can assuage some fear that the raw material could be out of specification or counterfeit from the start. Requiring raw material be sourced from an approved region can protect the purchaser from potential delays that could occur due to a failed mechanical or chemistry test. This also allows the purchaser to maintain a tighter control of custody of the order from start to finish. While there are benefits to specifying raw material be sourced from an approved region, the general trend is to specify that the material be manufactured and tested in an approved region.

As stated, mechanical and chemical tests are performed to ensure compliance with specifications. Tables 2 and 3 show samples of ASME requirements for SA-516-70 steel from the 2013 edition of ASME Section II. SA-516-70 is a common carbon steel plate found in pressure vessels.

Table 2. ASME Section II Mechanical Requirements [15]

Tensile Requirements of SA-516-70 Steel Plate	
Tensile strength, ksi	70-90
Yield strength, min, ksi	38
Elongation in 8 in., min %	17
Elongation in 2 in., min %	21

Table 3. ASME Section II Chemical Requirements [15]

Chemical Requirements of SA-516-70 Steel Plate	
Carbon, max:	
1/2 in. and under	0.27
Over 1/2 in. to 2 in., Incl	0.28
Over 2 in. to 4 in., Incl	0.3
Over 4 in. to 8 in., Incl	0.31
Over 8 in.	0.31
Maganese:	
1/2 in. and under	
Heat Analysis	0.85-1.20
Product Analysis	0.79-1.30
Over 1/2 in.	
Heat Analysis	0.85-1.20
Product Analysis	0.79-1.30
Phosphorus, max	0.035
Sulfur, max	0.035
Silicon:	
Heat analysis	0.15-0.40
Product Analysis	0.13-0.45

Mechanical and tensile test results are derived from testing done using material shaped to specific ASTM standards [10]. These samples are stretched using a tensile testing machine until they are stressed to their failure point. The final applied force is recorded to determine the material's tensile strength. Chemical testing is also performed by destructively testing sample material to determine the quantities of each element in the steel. It is important to note that both mechanical and chemical testing for ASTM standards are destructive processes. If a plate arrives at a fabrication shop with insufficient testing documentation, some of the material can be sacrificed to confirm mechanical and chemical properties. Confirmation of mechanical and chemical testing can only be done if the manufacturer has material to spare. Unlike plate and steel, with forgings there is rarely material to spare for testing purposes on a finished product.

Chemical testing for certain substances can be performed with a heat analysis or product analysis. Heat analyses are performed on an entire batch of materials that come from the same raw material billet. If many end products are made from the same material, a heat analysis is the more economical method. A product analysis is a chemical analysis of the semi-finished or finished product [9]. Because the product is closer to its finished state, a larger allowable range for certain elements is allowed to account for deviations associated with analytical reproducibility [11]. This is the benefit with using a product analysis. The cost associated with this benefit is that for a large batch of materials, a product analysis is more cost-prohibitive than a heat analysis.

Choice of analysis type makes no difference in the material content requirements for maximum carbon, phosphorus, and sulfur content. Carbon and manganese content, however, is affected by the thickness of the product.

Understanding how materials are manufactured is a key step in ensuring a quality final product. The purchaser should familiarize themself with specifications of materials that are ordered, and understand how materials tested, as well as what are considered the more critical manufacturing steps in production. By understanding how and why materials are tested, the purchaser can determine where additional quality assurance steps can reduce risk of substandard or counterfeit materials.

QUALITY MANAGEMENT

Once the purchaser understands how ordered material will be manufactured, a detailed quality management program can be outlined. As with any quality management program, the goal is to create a formalized process for ensuring results are consistent and in compliance with specifications. For steel plate, the final goal is a product that performs in compliance with the standards it was specified to. All steel mills have their own internal quality assurance practices; however, when purchasers buy product from a supplier or geographic region and do not have historical evidence of quality, as-specified products, it is often wise to perform additional testing and inspection as a safeguard.

One option that purchasers can use to ensure compliance with specifications is first or third party inspectors to review the fabrication process. An inspector may witness the entire fabrication process, or only the steps deemed most critical to final product integrity. Having inspectors witness the entire process ensures the chain of custody of materials from the heating of a slab through the final packaging and loading for shipment, but the cost of having this level of inspection would be quite high. This would be an effective quality program to be used when dealing with a potentially inferior manufacturer.

Purchasers must consider the additional costs of costs of these extra inspections when selecting a manufacturer. Purchasing from a manufacturer that a purchaser has not used before, and thus has no historical evidence of quality made products, adds inspection costs that could make an experienced manufacturer appear more cost effective.

Inspection of certain critical steps in the process is helpful when a purchaser's main concern is poor quality finished products. One step of high concern for steel plate

manufacturing is the heat treatment process. Having an inspector witness heat treatment helps to ensure that the manufacturing process complies with specifications. The cost of limited inspection is less than witnessing the entire manufacturing process; however, as the quantity of inspection hours are reduced, the higher the risk becomes that a finished product may be substandard.

A second option for quality management is to perform third party analysis of mechanical tests. Extra material or sample tabs can be manufactured, and extra test samples can be shipped to an independent laboratory. This proof testing adds additional costs, but these costs are typically much less than having an inspector in the shop full time.

Often times, substandard material is a symptom of a poor quality management program. The quality management program can be poor for very large processes like the manufacturing process outlined in Figure 1. Poor quality management programs can also stem from a buildup of simple problems such as poor document control and poor responsiveness to problems.

Purchasers can protect themselves from reusing a consistent bad vendor by creating an evaluation system for vendor criteria. Bernold and Treseler outline a prospective list of criteria to measure vendors [12]. These criteria are shown on Table 4. Keeping a log of vendor performance is beneficial, especially in a situation when lowest price is the largest determining factor of vendor choice. Using this type of evaluation system can prevent the purchaser from simply choosing the lowest-price vendor. The purchaser can eliminate or at least justify extra inspection or testing costs when purchasing from vendors that have shown poor workmanship in previous projects. Using this approach to selecting vendors makes it more likely that the true overall lowest cost vendor is selected.

CONCLUSION

Globalization has presented many new challenges to the steel industry, and possibly the greatest challenges posed are avoiding and detecting counterfeit and substandard materials. While the threats posed are great, the techniques outlined in this study, such as implementing additional quality assurance measures, can greatly reduce risk. Simple steps, such as understanding manufacturing processes, knowing how quality management is performed, and performing additional quality assurance when necessary can greatly reduce project risks. Proper quality management allows purchasers and end users to utilize low cost material and labor source countries to drive down overall project prices without, most importantly, reducing quality.

Table 4. Bernold and Treseler Vendor Performance Criteria [12]

List of Criteria with Relative Weights for Measuring Vendor Performance		
Criterion	**Weights for government contracts, %**	**Weights for commercial contracts, %**
Timeliness of submittals	15	10
Lead time for release	15	7
Response time to rejected submittals	6	4
Cooperation in overall planning	3	3
Cooperation in contacting engineer for approval	1	5
Cooperation in identifying deviations from specifications	5	1
Responsiveness to problems	7	7
Tracking of order	7	9
Time reliability	15	18
Cooperation of instructing installation	3	3
Expediting costs	3	6
Product quality	10	10
Timeliness and ability during startup	3	3
Production of operation and maintenance manuals	3	2
Responsiveness to warranty calls	4	12
Total	100	100

REFERENCES

[1] World Trade Organization, "Statistic Database," 2013. [Online]. Available: http://stat.wto.org/StatisticalProgram/WSDBViewData.aspx?Language=E. [Accessed 22 July 2013].

[2] World Trade Organization, "International Trade and Market Access Data," WTO, 1980-2012. [Online]. Available: http://www.wto.org/english/res_e/statis_e/statis_bis_e.htm?solution=WTO&path=/Dashboards/MAPS&file=Map.wcdf&bookmarkState={%22impl%22:%22client%22,%22params%22:{%22langParam%22:%22en%22}}. [Accessed 25 June 2013].

[3] O. G. Hatch, "Trademark Counterfeiting: Hearing Before the Committee on the Judiciary, U.S. Senate," Diane Publishing

Co., Darby, 1995.
[4] J. Hernandez, "Hollywood Man Sold Fake Parts To Military," Sun Sentinel, Fort Lauderdale, 2004.
[5] W. Stern, "WARNING! Bogus parts have turned up in commercial jets. Where's the FAA?," BusinessWeek, New York City, 1996.
[6] U.S. Customs and Border Protection Office of International Trade, "Intellectual Property Rights, Fiscal Year 2012 Seizure Statistics," Department of Homeland Security, Washington, D.C., 2013.
[7] P. C. i. L.-c. S. C. R. Team, "Product Integrity Concerns in Low-cost Sourcing Countries: Counterfeiting within the Construction Industry," Construction Industry Institute, Austin, 2010.
[8] P. D. C. Chow, "COUNTERFEITING IN CHINA AND ITS EFFECT ON U.S. MANUFACTURING," Columbus, 2004.
[9] ASTM International, Standard Specification for Common Requirements for Steel Flanges, Forged Fittings, Valves, and Parts for Piping Applications, West Conshohocken: ASTM International, 2012.
[10] ASTM International, Standard Test Methods and Definitions for Mechanical Testing of Steel Products, West Conshohocken: ASTM International, 2012.
[11] ASTM International, "Standard Test Methods, Practices, and Terminology for Chemical Analysis of Steel Products," ASTM International, West Conshohocken, 2011.
[12] J. F. T. Leonhard E. Bernold, "VENDOR ANALYSIS FOR BEST BUY IN CONSTRUCTION," American Society of Civil Engineers, Reston, 1991.
[13] World Steel Association, "Statistics archive," 2012. [Online]. Available: http://www.worldsteel.org/statistics/statistics-archive.html. [Accessed 2 July 2013].
[14] JFE Steel Corporation, "JFE Steel Plate Brochure," [Online]. Available: http://www.jfe-steel.co.jp/en/products/plate/catalog/c1e-001.pdf. [Accessed 15 June 2013].
[15] ASME, ASME Boiler and Pressure Vessel Code, Section II, Materials, Part A Ferrous Material Specifications, New York: ASME International, 2013.

MATERIAL CHARACTERIZATION OF NITINOL WIRES FOR THE DESIGN OF ACTUATION SYSTEMS

Sean P. Kennedy
Graduate Student
Mechanical Engineering Department
California Polytechnic State University
San Luis Obispo, California, United States

Dr. Saeed B. Niku
Graduate Advisor
Mechanical Engineering Department
California Polytechnic State University
San Luis Obispo, California, United States

ABSTRACT

A research project at California Polytechnic State University in San Luis Obispo, California is performing a series of tests on nickel-titanium alloy wire, also known as nitinol, to determine the plausibility of designing an actuator using this wire as the method of actuation. These tests have been designed to fully characterize how the wire behaves under steady state and transient conditions allowing for a specific wire selection to be made given known actuator specifications which will result in an efficient design. The wire transient data can be used to design a controller which reduces the actuation time. The research done for the overall project covers a wide scope including wire hysteresis, nitinol transition temperature, variable wire resistance, wire actuation as a function of current and pull force, cable fabrication, and wire actuation control to optimize performance. Through these tests, it has been determined that an actuator can be efficiently designed using this material.

INTRODUCTION

This study was initially introduced to give an alternative to motors which are commonly used for mechanical actuation. The advantage of motors is that much is known about how they behave, making other actuators less ideal. The purpose of this study would be to reduce the amount of unknown characteristics to nitinol wire, making it a more practical option.

Nitinol wire has the potential to be a preferred actuation method for certain applications given that it is a small, light, and relatively inexpensive material. Additionally, given known parameters to nitinol actuation wire can allow users to design their own specific actuator to meet their specifications.

BACKGROUND

Nitinol is a nickel-titanium alloy which is considered part of the shape memory alloy class which means that it goes through the shape memory effect as seen in Figure 1. When the material is held at low temperatures, it is in a very ductile form known as martensite. This allows for the nitinol wire to be bent

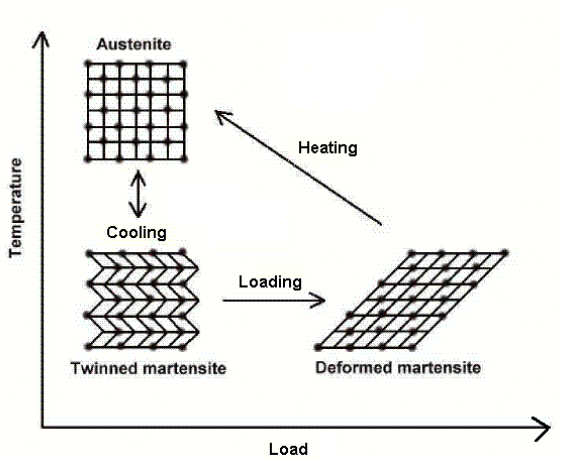

Figure 1. Shape memory effect [1].

in any shape. When the material is heated up past its transition temperature, it becomes much more rigid as it enters its austenite form. When nitinol wire enters the austenite state, it returns to its original shape regardless of any deformations that occurred at lower temperatures, therefore it is referred to as a shape memory alloy. When the material is cooled and re-enters its martensite state, it does not return to its deformed shape until a load is put on the wire [1].

Nitinol covers a wide range of nickel-titanium alloys with different nickel to titanium ratios. Given the specific composition, the characteristics will change. One notable characteristic is the temperature at which nitinol transitions between its martensite and austenite states. This will affect how useful nitinol is in certain situations. For example, in order to use nitinol as an actuator, the transition temperature must be above and differentiable from room temperature so that actuation can be controlled with the addition of heat. Specific samples of nitinol with transition temperatures below room temperature remain in the austenite form and thus can be used because of their rigidity.

The specific nitinol wire used in actuation application is sometimes referred to as Biometal™ and has special shape

memory properties. Pieces of Biometal™ wire have an austenite state which is a shorter version of the original wire, and therefore the wire will contract when heat is applied. When the wire contracts, it pulls with a certain amount of force. This pull force can be used as a method of actuation. When the heat is removed, the wire will return to its martensite state which will be the original length of wire, granted there is some restoring force in the wire. Unlike other types of nitinol wire, Biometal™ can be cycled millions of times between its martensite and austenite states which make it a desirable material for an actuator. The practical method to heating up Biometal™ wire is to apply a constant current through the wire [2].

Nitinol is primarily used in medical applications due to its superelastic properties and high corrosion resistance. Though there are some nitinol actuators currently being produced, they are much less common. The specific nitinol wires used for actuation in this series of tests is claimed to contract approximately 5-6% of its total length [3].

NITINOL TESTING OVERVIEW

At the start of the testing phase, it was important to identify what inputs and outputs would be essential to perform a complete and thorough analysis of nitinol wire. It was determined that the three primary inputs to consider would be wire diameter, current, and pull force. Two other inputs that could have been considered were nickel to titanium composition ratio and specific manufacturing process of the wire. These two additional factors will affect how the wire behaves, but given the scope for this project, it was determined that doing a complete study of nitinol provided by a single manufacturer would be sufficient. Also, there were only six wire diameters tested: 5, 6, 8, 10, 12, and 15 thousandths of an inch (mil) diameter wires.

The following variables were measured: wire contraction, temperature, wire hysteresis, current hysteresis, wire resistance, and time constants. Wire contraction and temperature are the most intuitive variables to observe as they are directly correlated to the input current. The wire hysteresis and current hysteresis are additional variables that were determined later in the testing process as it became evident that pull force had a large influence on the system outputs. The wire resistance was desired since many electromechanical applications are powered with voltage sources rather than current sources. The time constants are determined by the time required to actuate the nitinol wire.

TEST SETUP AND PROCEDURE

The same test setup, with some minor modifications for recording different variables, was used for most of the tests. A detailed schematic of the general setup can be found in Figure 2. Each piece of nitinol wire was clamped at the ends using spade lugs which could be easily clamped to a frame. One of the ends of the wire was attached to a replaceable spring that kept the nitinol wire in tension with a certain pull force. This spring was replaced for some tests whenever varying pull forces were desired. A variable constant current power supply

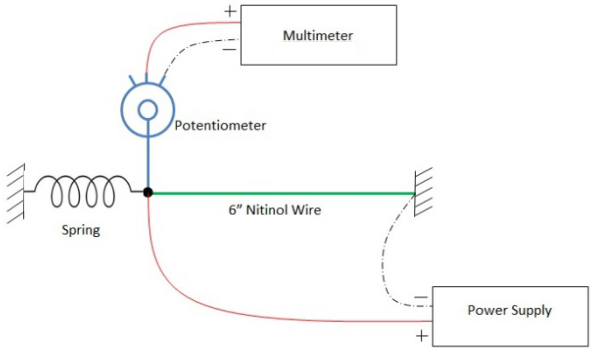

Figure 2. General test setup for all tests.

was used by attaching two probes at the two ends of the nitinol wire. This power supply also displayed the voltage drop across the nitinol which could be used to calculate the resistance of the wire during testing. A 5 kΩ rotary potentiometer was fitted with a lever arm that was attached to the connection between the nitinol wire and spring. Given that nitinol wire only contracts about 5% of its own length, the angular displacement measurement from the potentiometer could be converted to a linear displacement with negligible error. The output resistance from the potentiometer was read by a digital multimeter which was converted to a displacement given the geometry of the test setup.

Each individual test has a few minor alterations to record different variables using equipment such as a digital oscilloscope for the transient tests and a 10K3 thermistor, temperature sensor with 10 kΩ resistance at room temperature, for the temperature tests. Any variations to these tests will be described in the test section prior to discussing the results.

WIRE CONTRACTION TEST

By far the most important piece of information when using nitinol for mechanical actuation is how much the wire contracts when applying a varying current through the wire. By slowly increasing the current from a minimum to a maximum through its transition current and recording steady state displacements, a

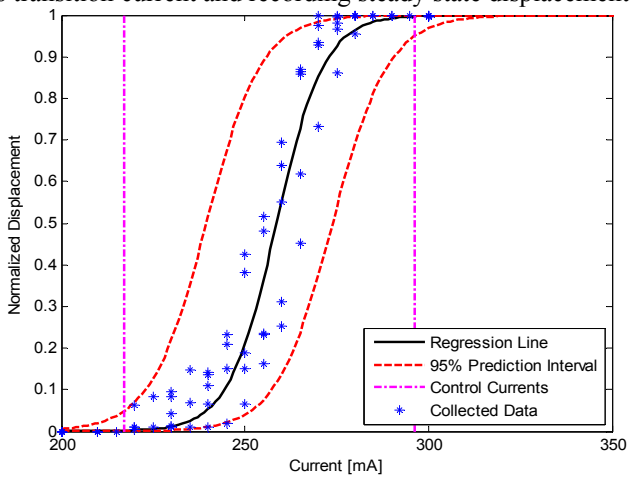

Figure 3. Wire contraction curve for 6 mil diameter wire.

regression curve can be made to fit the data allowing prediction of wire contraction as a function of current. This test was simplified by normalizing the wire contraction to eliminate the effect of wire hysteresis on this test. Figure 3 shows the results from this test for the 6 mil diameter wire. Results of other thicknesses are similar.

The results for this initial contraction test follow a logistic growth curve. A logistic growth curve is a type of non-linear regression line used in MINITAB®, a statistical software program where most data analysis was performed. The standard form of the logistic growth model is given by Equation 1:

$$y = C_1 + \frac{C_2 - C_1}{1 + e^{\left((x - C_3)/C_4\right)}} \qquad (1)$$

where, $C_1 \equiv$ the maximum value of y
$C_2 \equiv$ the minimum value of y
$C_3 \equiv$ value of x when y is halfway between C_1 and C_2
$C_4 \equiv$ a measure of spread in the x-direction

For this specific logistic growth regression, C_1 is 1 and C_2 is 0 since the normalized displacement ranges from 0 to 1. The value of C_3 represents the transition current where the normalized displacement reaches 50% or half of the total contraction. This regression line will be referred to as the contraction curve since the data was collected for increasing current values that cause the wire to contract.

Figure 3 also features a prediction interval, which is used to determine where 95% of the data is likely to fall. In practical use of nitinol, it is unlikely that all data points will follow the regression line exactly, so prediction intervals give a credible range of displacement values that can be expected for any current. Using these prediction intervals, two control current values were determined, which represent the current values where the nitinol wire is either fully extended or contracted. These current values are at the locations where the prediction interval range is 0.05 or 5% of the full contraction distance. These currents allow for a certainty in knowing whether or not the wire has contracted. At the upper control current, the nitinol wire is fully contracted. At the lower control current, the nitinol wire is fully extended. These control currents will be important when creating a control algorithm to decrease reaction times.

This initial curve does not characterize all contractions though. A study performed by Nitinol Devices and Components (NDC) shows a trend that data collected by heating the wire differs from the data collected by cooling the wire. NDC claims that there will be a gap between these two curves caused by hysteresis in the wire [4]. To test for this, the same test was performed with steady state measurements taken by slowly decreasing the current from a maximum to a minimum through the transition current. In fact, the data collected follows a new logistic growth curve with a lower transition current confirming this trend. This difference between transition current values for the contraction and extension curves will be referred to as current hysteresis, where the extension curve is the regression curve generated by data collected from decreasing current values that cause the wire to extend .

The current hysteresis was found to also be a function of the pull force. To test for this, the same test was performed multiple times with different springs to simulate different pull forces. Figure 4 shows the wire contraction test results performed with three different pull forces applied to the nitinol wire in grams.

The important observation is that the transition current for each extension curve approaches that of the initial regression curve, or the contraction curve. Even though the shape of each extension curve changes, it will be assumed that it does not change in order to simplify the final displacement model. Figure 5 shows these current hystereses plotted as a function of pull force as a means to approximate the current hysteresis for any pull force.

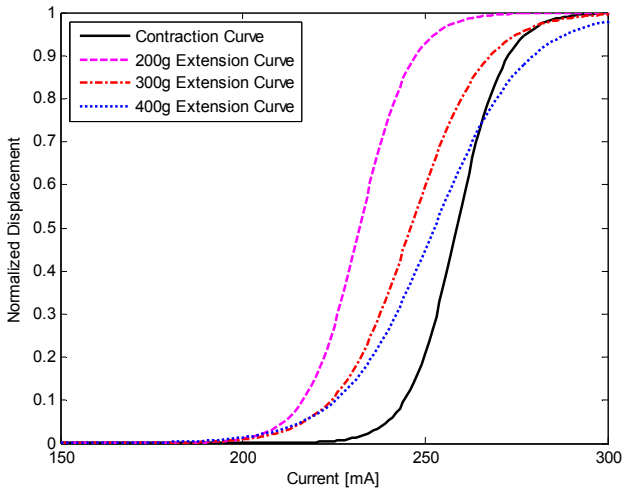

Figure 4. Wire contraction and extension curves for 6 mil diameter wire.

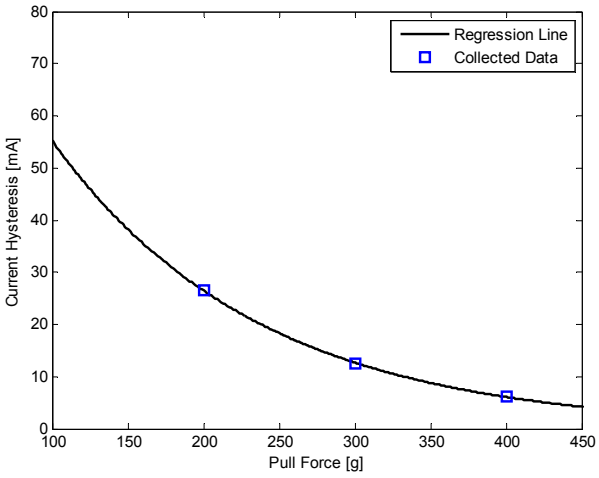

Figure 5. Current hysteresis as a function of pull force for 6 mil diameter wire.

WIRE HYSTERESIS TEST

The next set of tests was performed to determine how the contraction in the wire would be affected by pull force. This was done by measuring the contraction in the wire immediately after applying a pull force to the wire. To apply this pull force, the wire was removed from the setup and a weight was attached to one end of the nitinol wire with the other end fixed. Applying this force would extend the wire slightly if there was any hysteresis in the wire. Since the wire always contracts to the same length, the amount the wire contracted would represent a restoring displacement associated with the pull force applied prior to contraction. The wire hysteresis could be found by subtracting the restoring displacement from the total contraction displacement. This process was done for each wire at varying initial pull forces. As this pull force increased, the restoring displacement increased and the wire hysteresis decreased. Figure 6 shows the wire hysteresis as a function of pull force for the 6 mil diameter wire.

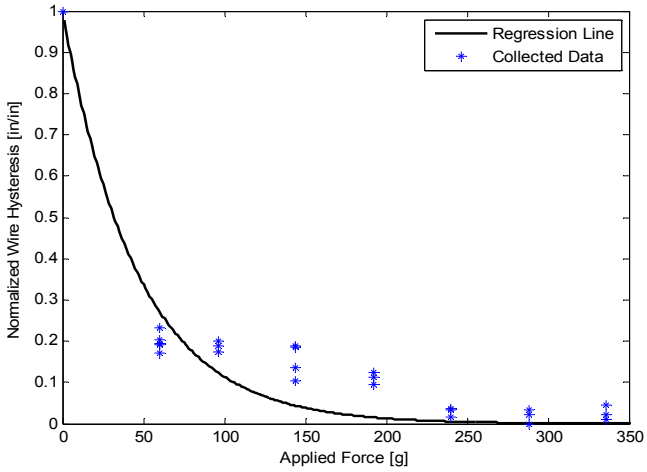

Figure 6. Wire hysteresis as a function of pull force for 6 mil diameter wire.

An exponential decay regression line was fit to the data in order to determine the amount of hysteresis that would be found in the wire for any applied pull force. This curve was also normalized between 0 and 1 to match the scale for the wire contraction test which also was normalized between 0 and 1. Using this scale allowed for easy development of the final displacement model.

FINAL DISPLACEMENT MODEL

Given the results from the wire contraction and wire hysteresis tests, a final model was made to fully characterize nitinol actuation displacement as a function of pull force and current. The logistic growth equations for the contraction and extension curves are shown in Equations 2 and 3:

$$\Delta l_{contract} = \Delta l_{max} + \frac{\Delta l_h - \Delta l_{max}}{1+e^{\left((I-I^*)/C\right)}} \qquad (2)$$

$$\Delta l_{extend} = \Delta l_{max} + \frac{\Delta l_h - \Delta l_{max}}{1+e^{\left((I-I^*+\Delta I_h)/C\right)}} \qquad (3)$$

where, $\Delta l_{max} = 0.066 \left[\frac{in}{in}\right]$

$\Delta l_h = \Delta l_{max} e^{-aF} \equiv$ Wire Hysteresis $\left[\frac{in}{in}\right]$

$\Delta I_h = \Delta I_{max} e^{-bF} \equiv$ Current Hysteresis [mA]

$F \equiv$ Pull Force [g]

$I \equiv$ Current [mA]

$\Delta I_{max} \equiv$ Maximum Current Hysteresis [mA]

$I^* \equiv$ Transition Current [mA]

$C \equiv$ Current Spread [mA]

$a \equiv$ Wire Hysteresis Decay Rate $\left[\frac{1}{g}\right]$

$b \equiv$ Current Hysteresis Decay Rate $\left[\frac{1}{g}\right]$

The required constants are found in Table 1. The value for Δl_{max} was found through testing.

Table 1. Constants for final displacement model.

Wire Diameter [mils]	ΔI_{max} [mA]	I* [mA]	C [mA]	a [g^{-1}]	b [g^{-1}]
5	152.3	213.6	8.66	0.01708	0.00860
6	115.1	258.6	6.47	0.02172	0.00735
8	265.1	331.7	8.93	0.00725	0.00542
10	199.8	437.3	16.92	0.00434	0.00080
12	335.5	578.5	26.68	0.00313	0.00039
15	393.5	706.6	28.12	0.00186	0.00018

These equations were created using the standard form of the logistic growth regression line including factors for wire hysteresis and current hysteresis. All the constants used in these equations were derived from regression lines from the wire contraction and wire hysteresis tests. I* and C come from Figure 3, ΔI_{max} and b come from Figure 5, and a comes from Figure 6.

MAXIMUM PULL FORCE

In addition to knowing how much the wire contracts, it is very important to know the maximum pull force in the wire. This will give the designer the ability to properly assess the mechanical work each wire can produce where work is force multiplied by displacement. Through careful analysis of what would be necessary in actuator design, it was determined that three distinct force values would be necessary for each wire: The maximum force before wire contraction starts to decrease (F_{max}), the minimum force to produce no wire contraction when the wire is heated (F_0), and the maximum force before wire failure (F_f). To obtain these forces, a piece of nitinol wire was fixed at one end with a weight attached to the other end. The wire was then contracted by applying a constant current through the wire using a power supply. The weight was then increased until there was a noticeable difference in the amount the nitinol wire contracted, this denoted the force F_{max}. The weight was then increased further until there was no noticeable contraction, this denoted the force F_0. The wire was then removed from the power supply and the weight was increased

until the wire failed, this denoted the force F_f. Figure 7 shows these three forces plotted against wire diameter.

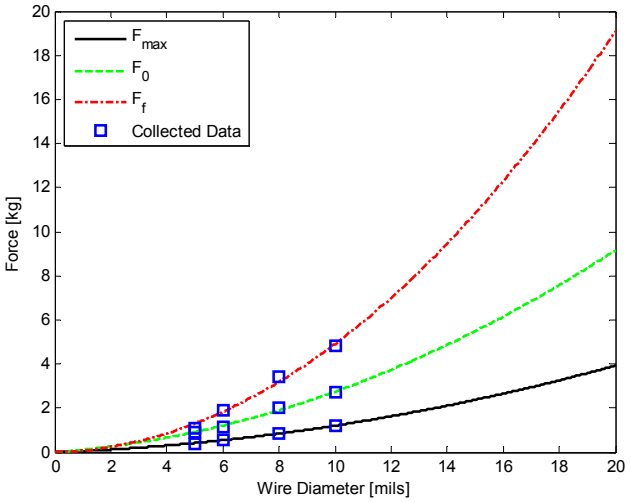

Figure 7. Force curves for any wire diameter.

Each of these three forces could be converted to a stress by dividing them by the cross sectional area of the wire. This stress should be constant from wire to wire, meaning that force should be linearly proportional to cross sectional area. Since area is a function of diameter squared, pull force will also be a function of diameter squared, which is why a quadratic regression line was used.

To interpret Figure 7, for any wire diameter, pull forces under F_{max} are desired as they do not reduce the amount the nitinol wire will contract. Pull forces between F_{max} and F_0 can be used, but will contract less resulting in less mechanical work. Pull forces between F_0 and F_f will result in no contraction and pull forces exceeding F_f will result in wire failure.

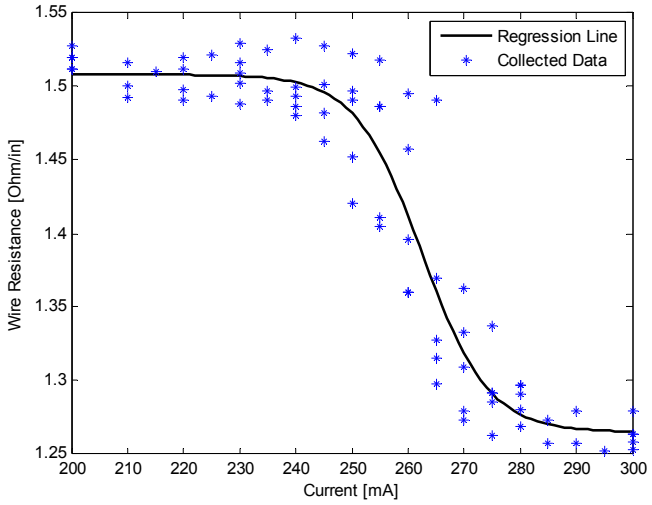

Figure 8. Resistance curve for 6 mil diameter wire for increasing current values.

VARIABLE WIRE RESISTANCE

Nitinol wire has a specific resistance value associated with its martensite and austenite crystal structures. If a voltage source is used to provide power to a nitinol actuator, it is very important to know these resistance values, since nitinol is current driven. It is interesting to note that not only are there two distinct resistance values, but there is also a similar logistic growth transition between them, similar to the regression found for wire contraction. Figure 8 shows the regression curve for the wire resistance in the 6 mil diameter wire that is associated with increasing current values that cause the wire to contract.

When this curve is compared to the logistic growth curve for wire contraction, the transition current and shape appear to be almost the same, so the same constants can be used for the resistance regression giving Equations 4 and 5:

$$R_{contract} = R_{min} + \frac{R_{max} - R_{min}}{1 + e^{\left((I - I^*)/C\right)}} \quad (4)$$

$$R_{extend} = R_{min} + \frac{R_{max} - R_{min}}{1 + e^{\left((I - I^* + \Delta I_h)/C\right)}} \quad (5)$$

where,

$\Delta I_h = \Delta I_{max} e^{-bF} \equiv$ Current Hysteresis [mA]
$F \equiv$ Pull Force [g]
$I \equiv$ Current [mA]
$\Delta I_{max} \equiv$ Maximum Current Hysteresis [mA]
$I^* \equiv$ Transition Current [mA]
$C \equiv$ Current Spread [mA]
$b \equiv$ Current Hysteresis Decay Rate $\left[\frac{1}{g}\right]$
$R_{min} \equiv$ Minimum Resistance [Ω]
$R_{max} \equiv$ Maximum Resistance [Ω]

The required constants are found in Tables 1 and 2.

Same as the final displacement model, I* and C come from Figure 3, and ΔI_{max} and b come from Figure 5. The two new variables R_{min} and R_{max} come from Figure 8.

Table 2. Resistance values for varying wire diameter.

Wire Diameter [mils]	R_{max} [Ω/in]	R_{min} [Ω/in]
5	2.131	1.823
6	1.501	1.266
8	0.812	0.692
10	0.544	0.467
12	0.359	0.310
15	0.292	0.269

TEMPERATURE TEST

In practice, nitinol wire is actuated by applying a current through the wire, but in theory, it is actuated by temperature; current is a means to heat up the wire to a specific temperature. From a design standpoint, it is important to know the

temperature an actuator will reach so the rest of the system can be designed with that in mind. The temperature of the wire is a function of resistance and current, I^2R, as this is the heat dissipation of the wire to the atmosphere. If nitinol had a constant resistance, one would expect temperature to be a quadratic function in terms of current. Given that nitinol has two distinct resistances, the temperature vs. current curve should have a parabolic shape on either side of the transition current where the concavity for larger currents is smaller given the decrease in resistance. In practice, a single cubic curve can be used to approximate the temperature for a reasonable range of currents for each wire. This cubic function for temperature is represented by the following equation that was generated using MINITAB®:

$$T = T_1 I^3 + T_2 I^2 + T_3 I + T_4 \qquad (6)$$

where T_1, T_2, and T_3 are cubic, quadratic, and linear coefficients determined by the cubic regression and T_4 is the constant term which is fixed at room temperature. For this regression, T_4 was fixed at 23.5 °C. Table 3 shows these constant values for all wire diameters.

To measure the internal temperature of the wire, a small thermistor was wrapped around the nitinol wire with the entire probe being in contact with the wire. Given that all nitinol samples used in these tests have a relatively small diameter when compared to the diameter of the thermistor probe, there will be some error in this method of data collection. To compensate for this error, temperature measurements were taken for all six wire samples and transition temperatures were found using the known transition current along with the cubic regression line. The maximum transition temperature was used as the true value since errors in temperature measurements are most likely to decrease the recorded temperature. Each regression line was then compensated by changing the linear component, T_3, so that the true transition temperature would occur at the transition current for each wire. The smaller diameter wires needed the most compensation since it was harder to get an accurate reading on such small diameter wires. Figure 10 shows the temperature curves for the 6 mil diameter wire which yield a final transition temperature of 67.4 °C.

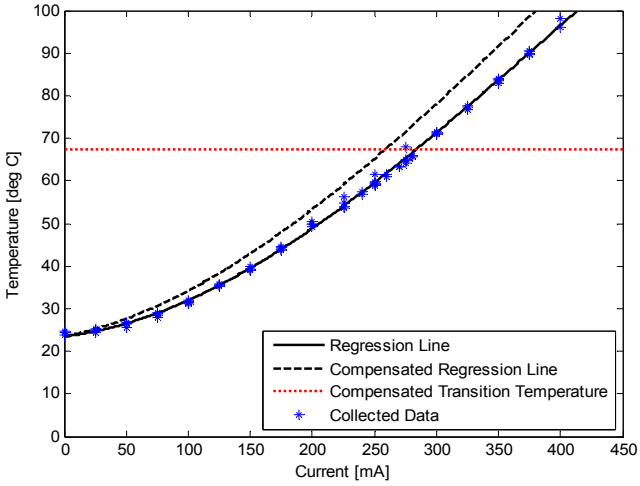

Figure 10. Compensated and uncompensated temperature curves with transition temperature for 6 mil diameter wire.

Knowing the transition temperature can help determine the nickel to titanium ratio. More research was done by NDC to create a correlation between nitinol transition temperature and Nickel to Titanium ratio as seen in Figure 9. It is estimated that this ratio is about 0.98 for the samples of wire tested. This ratio will definitely affect the transition temperature of nitinol, but it may also have an impact on other characteristics such as wire time constants and max pull force.

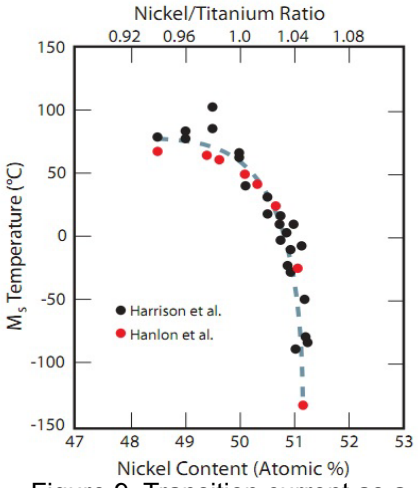

Figure 9. Transition current as a function of Nickel to Titanium ratio [4].

Table 3. Constants for temperature curve found from the compensated regression curves.

Wire Diameter [mils]	T_1 [°C/mA^3]	T_2 [°C/mA^2]	T_3 [°C/mA]	T_4 [°C]
5	-8.40E-07	9.18E-04	0.0475	23.5
6	-4.75E-07	5.64E-04	0.0555	23.5
8	-1.23E-07	2.92E-04	0.0489	23.5
10	-8.62E-08	2.05E-04	0.0274	23.5
12	-6.59E-08	1.52E-04	0.0100	23.5
15	-4.42E-08	1.12E-04	0.0050	23.5

TRANSIENT TEST

Thus far, all presented results relate to steady state values with no regards to any transient effects. This following test was designed to determine the time constants for each of the wires so that total reaction times could be determined. This test used the same general setup as the wire contraction test with the addition of two oscilloscope probes that were used for triggering and data collection. The first set of oscilloscope probes was put across the power supply which was used to trigger data collection. The second set of oscilloscope probes was placed across the potentiometer leads. Since the oscilloscope measures voltage drops and not resistance, a small circuit was created by placing a 2.7 kΩ resistor in series with the potentiometer leads and a 5V voltage drop across these two resistances. The voltage measured by the second oscilloscope is

Table 4. Contraction and extension time constants.

Wire Diameter [mils]	Contraction Time Constant [s]	Extension Time Constant [s]
5	1.472	1.102
6	1.087	1.100
8	1.157	2.009
10	1.261	3.521
12	1.343	5.841
15	1.782	9.936

representative of the length of the wire and can be used to record changes in length with respect to time.

To determine the time constants for each wire, a constant current was applied to each wire while the oscilloscope recorded the transient effects. The time required to fully contract the wire would be representative of twice the time constant at 95% contraction level. This test was also performed by cooling wires down by removing the current applied to the wire and recording the transient effects. Each wire has two time constants, one for the increasing currents and one for decreasing currents. Table 4 shows the two time constants for each wire. It is important to note that all transient results were at room temperature without the aid of any fluid bath or air convection to decrease the time required to cool the wire.

During this test, it was observed that each wire would not immediately contract when current was applied. This is due to the fact that it takes time for the wire to reach the transition temperature when it starts contracting. It was theorized that if the wires were partially heated, they would contract much more quickly. Each of the transient tests was repeated with adjusting the initial current to pre-heat the wire before contraction and extension. In every case, the time to contraction/extension was decreased by altering this initial current. This trend can be seen in Figures 11 and 12. These figures do not show the total contraction and extension times, but the time prior to contraction or extension.

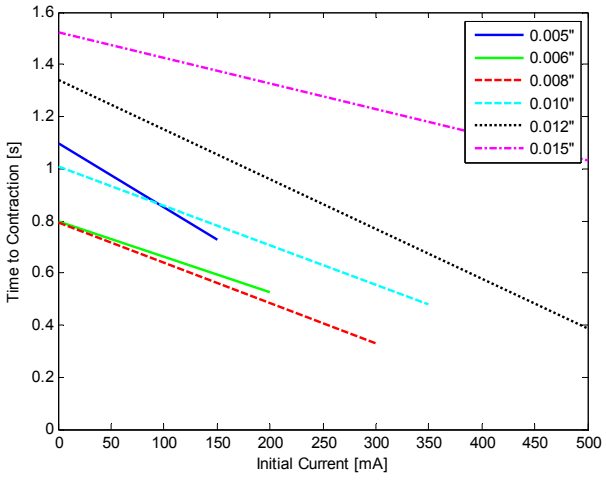

Figure 12. Time to contraction values at varying initial currents.

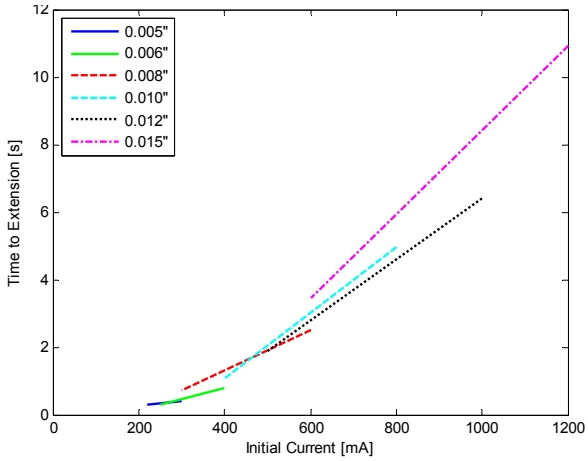

Figure 11. Time to extension values for varying initial currents.

CONTROL ALGORITHM

Given that decreasing the starting current prior to actuation can reduce reaction times, one might ask how to design the most efficient control algorithm to reduce reaction times to a minimum. Using the control currents and current hysteresis found through the wire contraction tests along with the time constants found through the transient tests, a precise control algorithm can be constructed. A crude graphical model of this control algorithm can be found in Figure 13.

In this figure, the current is adjusted between four distinct current values: maximum current (I_{max}), upper control current (I_{UCC}), lower control current (I_{LCC}), and off. The upper control current is found directly from the prediction interval of the initial wire contraction test. The lower control current is found

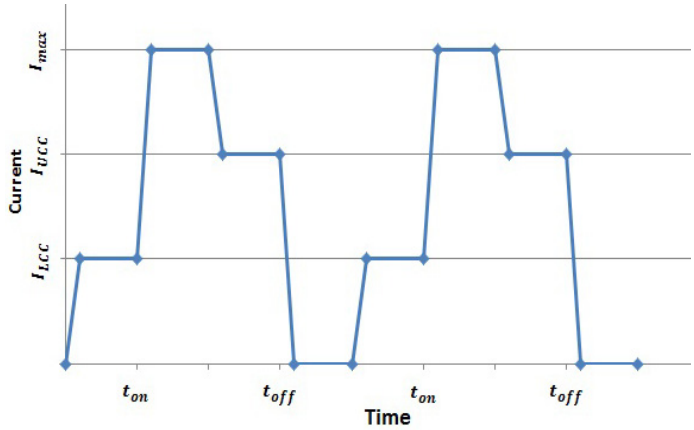

Figure 13. Control algorithm used for an efficient actuator design.

by subtracting the current hysteresis from the control current found in the initial wire contraction test. This will account for any current hysteresis caused by small pull forces. The maximum current is found through the temperature curves so that a certain temperature is not exceeded in the nitinol wire. A maximum current is selected primarily to ensure the nitinol

Table 5. Current values used for control algorithm.

Wire Diameter [mils]	I_{max} [mA]	I_{UCC} [mA]	$I_{LCC} + \Delta I_h$ [mA]
5	355	277	160
6	438	296	217
8	542	396	262
10	727	576	317
12	1004	742	405
15	1253	852	576

wire does not exceed a certain temperature. Though no maximum temperature was determined to be the absolute maximum, it is advised not to exceed 120 °C. Table 5 shows these currents used in the control algorithm.

Note that I_{max} is based on a maximum temperature of 120 °C and $I_{LCC} + \Delta I_h$ is the lower control current before subtracting the current hysteresis found in Table 5. This current hysteresis will be a function of the pull force as previously mentioned.

The control algorithm is performed by going through the following steps:

1. When the nitinol wire is fully extended at room temperature, the current through the wire is raised to the lower control current. This will heat up the wire without causing any actuation to occur.
2. When the nitinol wire needs to be contracted, the current through the wire is raised to the maximum current for the wire. This will rapidly heat up the wire through its transition temperature resulting in a quick response.
3. Once the wire if fully contracted, the current through the wire is lowered to the upper control current. This will cool down the wire without causing any actuation to occur.
4. When the wire needs to be extended, all power is removed from the wire. This will rapidly cool down the wire through its transition temperature resulting in a quick response.
5. Repeat process as necessary.

If this process is used, a nitinol actuator will have a relatively quick response limited only by the time constant of the wire itself.

CABLE FABRICATION

For mechanical applications where large pull forces are required, a single piece of nitinol wire will not be enough. Cable fabrication becomes a desired approach and offers some advantages to single large diameter wires. Cables are much more flexible than a single strand and can be used in applications such as pulley systems. An extra advantage is that creating a cable of smaller wires allows for easier clamping of the wire. For a single strand, a clamp must hold onto a small wire with a very large amount of force, whereas for a cable of wires, a single long strand can be wrapped into a coil providing loops of nitinol that can be used for clamping.

Given the shape memory property of nitinol, it is very easy to make a cable. By twisting several strands of nitinol together and heating them up to their austenite state while held in tension, they will stay in that same shape when cooled down to their martensite state. As long as there is always some tension in the cable when they are heated up, they will continue to hold their shape making braiding of wires unnecessary.

Some of the tests in this study were repeated using cables to see how they performed when compared to single cables of similar cross sectional area. It was found that these cables behaved very similarly to single wires, which means the results obtained through these tests will also apply to cables. These similarities include cables holding proportionally larger loads and cable resistances being modeled as single wires in parallel. These characteristics offer a wide range of options when compared to using a single wire in an actuator design.

INTERPRETATION OF RESULTS

If the wires used during this study were directly applied to a nitinol actuator, the results obtained could be directly applied as well. Unfortunately, given that the nickel to titanium ratio is unknown and may affect the tests performed, the results presented may not be numerically accurate for all wires. On the other hand, all trends found in this study should hold true for any nitinol wire. It is recommended that any wire being used for actuation go through a brief set of tests to determine the numerical values for transition current and maximum pull force. As discussed in the temperature test section, wires with a nickel to titanium ratio of about 0.98 are more likely to have numerical results similar to the ones found in this study, but this has not been confirmed. Additionally, the method of fabrication of the wire itself may affect the behavior of each wire. This unknown factor is expected to be the cause of inconsistent data found in this study.

CONCLUSION

Through a careful analysis and testing of nitinol wire, it was determined that an actuator could in fact be designed using nitinol as the method of actuation. Also, it has been determined that a careful control algorithm can be implemented to decrease reaction times resulting in a more efficient design. Nitinol wire can be implemented in any actuator design, allowing for customizable specifications giving nitinol actuation an edge to other methods for certain applications.

REFERENCES

[1] Ryhänen, J., 1999, “Biocompatibility evaluation of nickel-titanium shape memory metal alloy,” Ph.D. thesis, University of Oulu, Rautaruukki, OY, Raahe, Finland. pp. 26-27.
[2] Biometal™. Toki Corporation, Japan. 1987. VHS.
[3] "Nitinol/Flexinol® Actuator Wire." Images SI Inc., 11 July 2013. http://www.imagesco.com/articles/nitinol/04.html
[4] Duerig, T., Pelton A., and Trepanier C., 2011, “Nitinol,” ASM International, SMST e-Elastic newsletter. pp. 2-3,22-23.

THERMOELECTRIC AND MECHANICAL PROPERTIES OF SIC+SWCNTS+B_4C NANOCOMPOSITES WITH SOL-GELS DIFFUSION

Mujibur R Khan, Maxwell Friel, Jabeous Weaver
Department of Mechanical Engineering,
Georgia Southern University, Statesboro, Georgia, USA

ABSTRACT

Thermoelectric (TE) and mechanical properties of Single wall carbon nanotubes (SWCNTs) and Boron Carbide reinforced Silicon carbide (SiC) nanocomposites were experimentally evaluated after doping through the sol-gel diffusion technique. The samples were produced with a high temperature (1550^o C) sintering process. For sol-gel diffusion, a Boron-Antimony combination was used. Boron (B) was a P-type and Antimony (Sb) was an N-type dopant. Hot and cold junctions were created using silver epoxy and Alumel (Ni-Al) wire, and thermoelectric tests were conducted. The carbon nanotubes used were approximately 60% semiconducting and 40% metallic. Voltage (mV) was measured for different categories of samples against temperature difference (ΔT). Control SiC samples showed no TE effect at pristine form, but when infused with SWCNTs, a TE effect was present. The TE effect of the nanocomposite samples increased substantially with Boron-Antimony sol-gel diffusion. The Seebeck coefficient increased to 1.2 mV/ ^{o}C. Three point bending tests of the nanocomposites samples showed an interesting plateau in the flexure stress-strain curves. The structure-property relation was analyzed using SEM (scanning electron microscope) and EDS (Energy dispersive spectroscopy). It was revealed that fiber-like SWCNTs created a randomly distributed network, and Nano bridges inside the SiC matrix and enhanced the thermoelectric and mechanical properties of the nanocomposites.

INTRODUCTION

Ceramic materials (such as SiC) are attractive structural materials for high temperature applications because of their excellent mechanical strength, thermal stability and corrosion resistance. Despite these advantages, ceramic materials are susceptible to fast fracture due to their inherent brittle nature. A literature survey has revealed that fiber reinforced SiC matrix composites exhibit improved bending strength and fracture toughness as compared to monolithic SiC. For example, SiC_f/SiC nanocomposite exhibits a bending strength of 600 MPa and flexural strength of 5.5 MPa.m$^{1/2}$, both are ~ 20% more than the values exhibited by monolithic SiC [1-3]. Carbon fiber reinforced SiC nanocomposites show similar enhancement of bending strength and fracture toughness. Although the mechanical properties are improved, transverse thermal conductivity shows a decrease in fiber reinforced SiC composites as compared to monolithic SiC. A high-purity SiC has a room temperature thermal conductivity value of > 300 W/m-K, whereas, the conductivities of SiC_f/SiC composites have been observed to be between 30-70 W/m-K [1, 4].

Recently, carbon nanotubes (CNTs) are gaining tremendous interest due to superior mechanical strength and elastic modulus, excellent thermal conductivity and extremely low electrical resistivity. The strength and modulus of SWCNT have been reported to be as high as 200 GPa and 1.5 TPa, respectively [1, 5]. Literature data shows that the incorporation of CNT improves both bending strength and toughness by 10% over monolithic SiC at 2000^{o}C. Further enhancement (~ 14.5%) can be achieved by coating the CNTs with SiC and use it as reinforcement into SiC matrix. SWNTs can have a thermal conductivity as high as 3500 W/m-K along the tube's axis [6], which is almost an order higher than that of SiC.

The high thermal conductance of CNTs suggests that their incorporation might improve the conducting properties of SiC/CNT nanocomposites, however experimental data are not available [7]. It has also been reported that SWCNTs are thermally stable up to 2800^{o}C in vacuum [8]. However, CNTs are vulnerable to oxidation and hot corrosion at high temperature. To prevent CNTs from oxidation under hot corrosive environment researchers have coated CNTs with SiC. It has been reported that CNTs can sustain as high as 1600^{o}C without oxidation when coated with a very thin layer (30-50 nm) of SiC [9]. Metallic CNTs can carry an electric current density of 4 × 109A/cm^2. The resistivity of SWCNTs can be as low as 10^{-6} Ω-cm compared to that of SiC (10^2 – 10^6 Ω-cm). Moreover, experimental results revealed that their conductivity increases with increasing temperature from 456.6 S-cm^{-1} at 75.4 K, to 595.2 S-cm^{-1} at 300 K [10, 5]. All these extraordinary properties make CNTs ideal candidates for the preparation of high-performance ceramic nanocomposites with multi-functional properties.

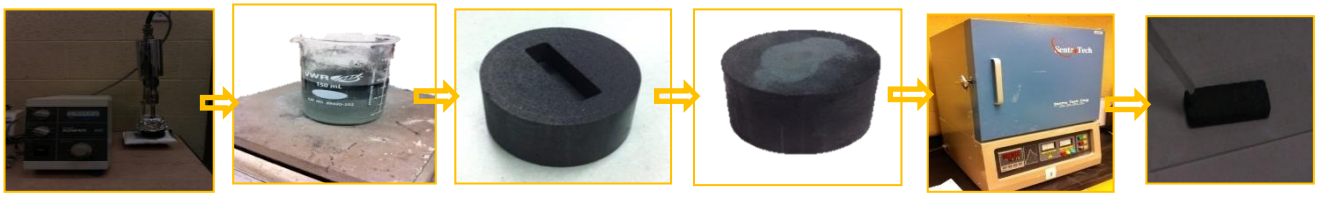

Figure 1: Fabrication of the nanocomposites samples

Recently, our group have been investigated the thermo- electric properties of SWCNTs and SiC nanoparticles. SiC nanoparticles showed no TE effect. However, when mixed with SWCNTs, significant TE properties were observed. With the addition of 5-10% SWCNT, the Seebeck coefficient and current have been increased to almost 0.1 m V/^{o}C and 10 µA, respectively [11-13]. These results indicate that SiC/SWCNT nanocomposites have the potential to generate significant TE effect. Moreover it has been reported that damage accumulation in CNT reinforced structural composites cause resistive heating (the Joule effect heating) and change the TE properties of the material [14]. The goal of this paper is to experimentally investigate the thermoelectric properties of SiC and SiC+SWCNTs+B_4C nanocomposites with and without sole-gels (Boron - Antimony) diffusion. Flexure stress-strain behaviors of the nanocomposites and the control samples have also been investigated. Experimental section describes the details of the sample preparation, thermoelectric and flexure test procedures of the control and nanocomposites samples. Experimental section is followed by the results and discussion to characterize the structure-property relationship. Finally a conclusion of our findings is provided.

EXPERIMENTAL

In order to produce the SiC+SWCNT+B_4C nanocomposites, a high-temperature sintering technique was used. At first, CNTs were homogeneously dispersed in ethanol solvent using an ultrasonic bath and horn sonicator. The sonication intensity was maintained at a level that does not cause damage or defects in the nanostructure of the nanotubes. SiC and B_4C powders were then mixed with the nanotubes suspended in solvents and homogenized using a homogenizer. The wt. % of SWCNTs and B_4C were 5.0% and 1.0%, respectively of the matrix material SiC. B_4C was used as sintering additives. The average particle size of B_4C was 10 µm. It has been reported that using B_4C as additives the relative density of SiC-CNT nanocomposites increased to 98% of theoretical density [15]. The produced slurry was then transferred to a desiccator to be de-aired and then dried around 60 -70^{o}C for prolong time to evaporate the solvents. The final composites were produced using high temperature sintering method based on a high-temperature consolidation. Such process can rapidly consolidate powders through the effects of rapid heating.

To sinter the composite sample, a die was prepared using graphite solid tube. The tube was approximately 2.5 inch in diameter. A rectangular shape hollow was machined at the middle of the graphite tube, as can be seen in Fig 1 with desired dimension. The mixtures were then poured into the hollow of the graphite and rammed properly to facilitate solidification. The graphite die was then placed into the chamber of a Sentro Tech high temperature furnace. The furnace was heated to 600 ^{o}C for a short time and then ramped at a rate of 10^{o}C/min to 1550^{o}C, and that temperature was held for approximately 20 hours. The furnace was automatically controlled and cooled down to room temperature at a cooling rate of not more than 10

Figure 2: Doping of samples using sol gel diffusion technique

^{o}C/min. The consolidated nanocomposite sample was then separated from the die and cut into the desired dimension (25 mm × 3.0 mm × 2.0 mm) using a diamond cutter according to ASTM C 1341-97. Figure 1 shows a scheme of the sintering process.

Once the composite samples were ready, sol-gels were spread on the samples (Fig. 2). The sol-gel coated samples were then heated inside a tube furnace at around 800^{o}C for 8-9 hours under Argon environment. Half of the sample area was diffused with Antimony (Sb) sol-gel and the other portion was diffused with Boron (B) sol-gel. Antimony was a N-type and Boron is a P-type dopant.

Once the sample was ready, a thermoelectric circuit (Figure 2) was prepared using Alumel (Ni-Al) wire and conductive silver epoxy. Junctions between samples and Alumel wire were created using conductive silver epoxy at the two ends of the sample. One of the junctions was then placed on a hot plate (CRHP-12650/230-E-A), with a temperature controller. The other junction was kept on top of an ice bag to maintain low

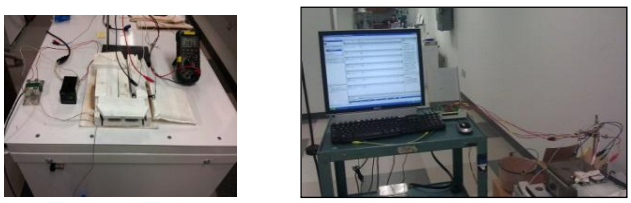

Figure 3: Thermoelectric tests of the samples

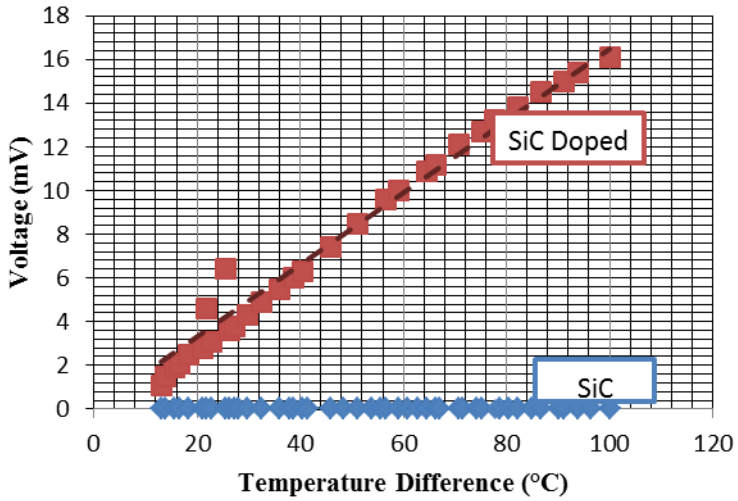

Figure 4: Voltage vs. temperature difference of SiC and doped SiC

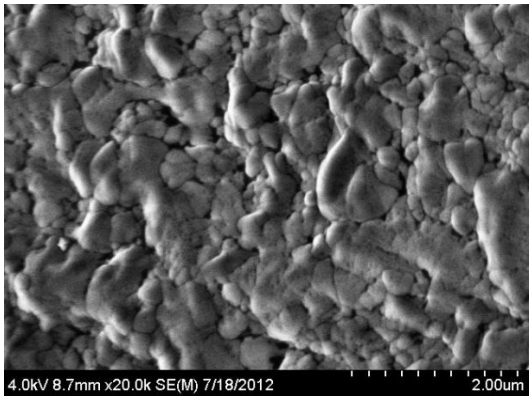

Figure 5: SEM micrograph of closely packed SiC sample

temperatures. The Alumel wires were long enough and one of the ends of the Alumel was connected with the connecting wires of the data acquisition system. Two thermocouples were placed at both hot and cold junctions to measure the temperature difference (ΔT). These thermocouples were also connected to the data acquisition system. Properties such as voltage as a function of temperature difference of the hot and cold junctions were recorded. The flexural stress and strain of the produced samples were investigated by three point bending test using an MTS universal testing machine. The flexural strength was derived from the load-displacement curve of the three point bending tests according to ASTM C 1341-97.

RESULTS AND DISCUSSION

The Seebeck coefficient for neat SiC and doped with Boron–Antimony (B-Sb) sol-gels, was measured from the voltage vs. temperature difference curve, as can be seen from Fig. 4. It has been observed that the neat SiC samples did not show any Seebeck coefficient. A very high energy band gap (4.9 eV) and resistivity (10^6 Ω-cm) are probably the reasons why it did not show any significant thermoelectric effect at the given temperature difference. However, when the SiC sample was doped with B-Sb, the Seebeck coefficient was 0.16 mV/°C.

It is expected that P-type boron dopant and N-type Sb dopant placed side by side, create an area of excess electrons and area of deficiency of electrons which facilitate the thermoelectricity to be generated to some extent. Figure 5 shows a micrograph of a closely packed SiC sample. Figure 6, shows a micrograph of a SiC sample which has been treated with the sol-gel (B-Sb). From this picture it is not clear if a chemical doping has occurred. However, presence of a foreign particulate such as Sb has been identified through EDS analysis. The presence of Gold (Au) has been identified due to the gold coating that was found during the SEM tests. Figure 7 shows the voltage and temperature difference curves for the doped and undoped SiC+B_4C(1%)+SWCNT(5%) nanocomposites. The Seebeck coefficient was about 0.25 mV/°C for the SiC+B_4C (1%)+SWCNT(5%) samples. It has been observed that the Seebeck coefficient of the

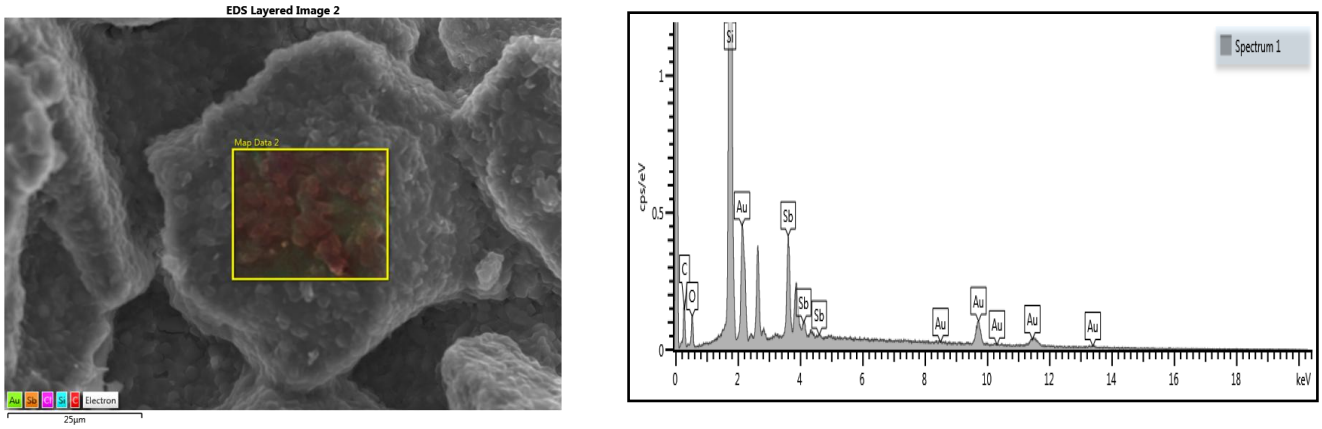

Figure 6: SEM micrograph and EDS analysis of a loosely packed SiC samples doped with sol-gels

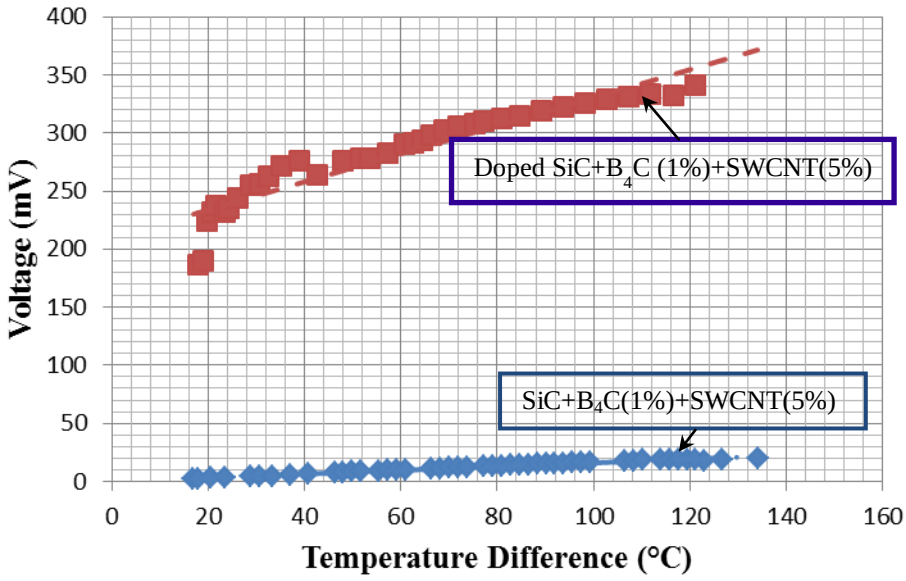

Figure 7: Voltage vs. temperature difference of doped and undoped SiC+B_4C (1%)+SWCNT(5%)

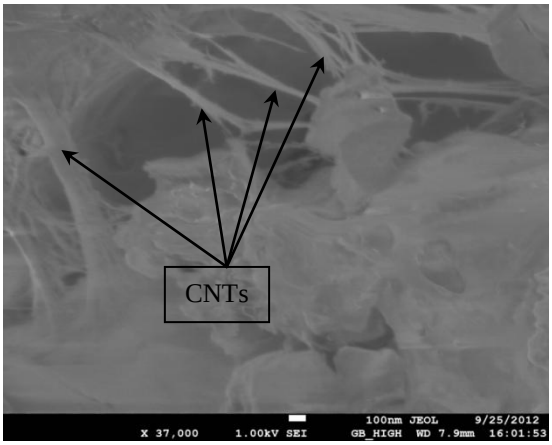

Figure 8: SEM micrograph CNTs creating bridges between the SiC particles

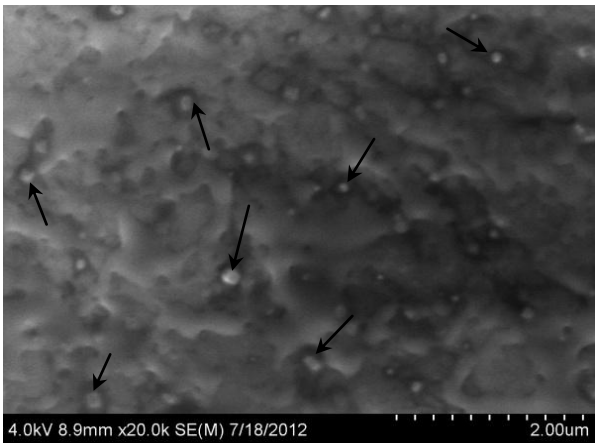

Figure 9: SEM micrograph of doped SiC+B_4C (1%)+SWCNT(5%)

nanocomposite even without the sol-gel doping is higher than that of SiC doped with B-Sb. However, when doped with B-Sb sol-gels, the SiC+B_4C(1%)+SWCNT(5%) nanocomposite sample showed significantly improved Seebeck coefficient. The Seebeck coefficient was approximately 1.2 mV/^{o}C in this case.

We attribute this improvement both due to the presence of SWCNT and the dopant effect. In our previous experiments [11-13], it has been shown that a randomly distributed CNT network can significantly enhance the thermoelectric effect by creating nano contact junctions. These junctions play an important role to create the thermoelectric effect in the combined material systems (SiC+SWCNT). We believe these nano junctions disrupt and break the electron hole symmetry of the nanotubes, which results in a thermoelectric effect through the electron drift and phonon drag effect. It has been reported earlier that the assembly of individual (10, 10) tubes into a rope is sufficient to break the single-tube electron-hole symmetry [16]. An interaction can change the dimensionality of the electronic structure breaking the electron-hole symmetry by causing an energy dependence of the density of states and the area of the Fermi surface. The work has predicted that tube-tube interactions in a rope of (10, 10) tubes cause the opening of a "pseudogap" in the density of states of the rope at the Fermi level. Symmetry breaking such an interaction mechanism caused the thermopower from both drift and phonon-drag effects [17]. Similarly it has been also reported that strong junction potential of carbon tube fin array was the key parameter controlling the energy conversion efficiency. The NJ system promises a high efficiency (~40% or higher) for thermal

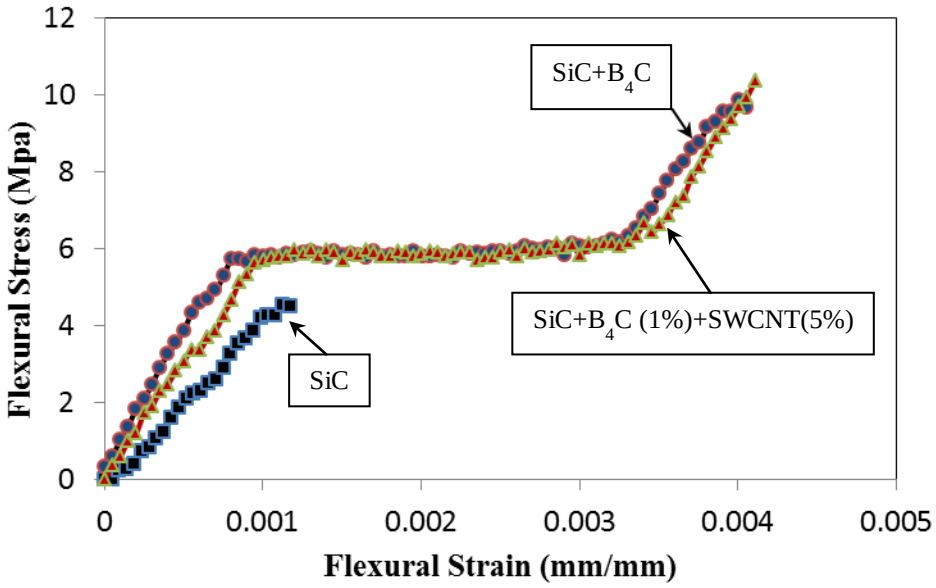

Figure 10: Flexural Stress-strain curves for different categories of samples

and electric energy conversion [18]. It has also been shown that, when the nanotubes are doped with B-Sb sol-gels, the enhancement of Seebeck coefficient is significant. Figure 9 shows a SEM micrograph of a doped SiC+B_4C(1%)+SWCNT(5%). It is to be mentioned here that B_4C was used in the nanocomposites to have a binding effect between the matrix and the nanoparticles. Figure 10 represents the flexure stress and strain curves for different catagories of samples. Flexure stress has been derived from the load-displacement curve of the three point bending tests according to ASTM C1341-97. The samples were tested without any sol-gel dopants. It is evident from Fig. 10 that the neat SiC sample tends to be very brittle and fractured at an early stage. However, both SiC+B_4C(1%)+SWCNT(5%) and SiC+B_4C(1%) composite samples showed some degree of deformation ability as can be marked by the plateau in the stress-strain curve. It has been also observed that the stress level has been increased even further after the plateau. It is clear from the curves that both flexure strength and modulus increased in the composite samples compared to neat SiC. The prolonged deformation ability marked by the observed plateau indicates some degree of plasticity in the composite samples.

CONCLUSION

SiC+B_4C(1%)+SWCNT(5%) nanocomposites were prepared through high temperature sintering process. Control SiC samples were also prepared. Samples were doped using sol-gels (B-Sb) diffusion. Thermoelectric and Flexure tests were conducted. Seebeck coefficient increased remarkably with presence of SWCNT and doping simultaneously. Flexure tests revealed that flexure stress and modulus increased substantially with prolong deformation characterized by stress-strain plateau in the composite samples. On the other hand, control SiC samples showed brittle behavior under flexure loading.

Acknowledgements: The Authors would like to acknowledge the support from the Startup grant From Mechanical Engineering Department at Georgia Southern University.

References:

[1] S. C. Tjong, Carbon Nanotube Reinforced Composites-Metal and Ceramic Matrices, Wiley-
VCH, Weinheim, 2009.
[2] W. Kowbel and C. A. Burce and K. L. Tsou and K. Patel and J. C. Withers and G. E.Youngblood, High thermal conductivity SiC/SiC composites for fusion application, J. of Nucl.Mat. 283-287 (2000) 570-573.
[3] A. Hasegawa and A. Kohyama and R. H. Jones and L. L. Snead and B. Riccardi and P. Fenici, Critical issues and current status of SiC/SiC composites for fusion, J. Nucl. Mat., 283-287 (2000) 128-137.
[4] G.E. Youngblood and D. J. Senor and R. H. Jones and S. Graham, The transverse thermal
conductivity of 2*D* − *SiC*$_f$*/SiC* composites, Comp. Sci. and Tech., 62 (2002) 1127.

[5] Yury Gogotsi,Nanomaterials handbook, Taylor and Francis, FL, 2006.
[6] P. Eric and M. David and W. Qian and G. Kenneth and D. Hongjie, Thermal conductance of an individual single-wall carbon nanotube above room temperature, Nano Letters, 6 (2005) 96.
[7] W. A. Curtin and B. W. Sheldon, CNT-reinforced ceramics and metals, Materials Today,
Review Feature (2004) 44-49.
[8] E. T. Thostenson and C. Li and T.W. Chou, Nanocomposites in context, Composites Science and Technology, (2005), 65, 491-516.
[9] Research on Carbon Nanotubes and Composites, Pan Group, Faculty of Engineering Department of Physics and Astronomy, University of Georgia.
[10] B. Bhushan., Springer Hand book of nanotechnology, 2010, Springer,Columbus, Ohio
[11] O. Garcia, M. R. Khan, A. R. Choudhuri, N. Love "Experimental Study of Thermoelectric Properties of Randomly distributed CNTs and SiC Nanoparticles" Terrestrial Fossil Energy Systems,AIAA JPC/IECEC, 2012 Conference, Atlanta, Georgia.
[12] A. Chowdhury, O. Garcia, M. Khan, L. Cabrera, Thermoelctric properties of Carbon nano tubes, Novel Testing and Materials, 2nd southwest energy science and engineering symposium El Paso, Texas, March, 2012
[13] L. Cabrera, O. Garcia, M. Khan, A. Chowdhury , Investigation of thermoelectric properties of SiC+SWCNT, Energy Materials Technology, 2nd southwest energy science and engineering symposium, El Paso, Texas, March, 2012
[14] R. G. Villoria, N. Yamamoto, A. Miravete and B. L. Wardle Multi-physics damage sensing in nano-engineered structural composites, Nanotechnology, 22 (2011) 185502.
[15] R. Z. Ma, J. Wu, B. Q. Wei, J. Liang, D. H. Wu, Processing and properties of carbon nanotubes-nano-SiC ceramic, Journal of Material Science 33 (1998) 5243 -5246
[16] J. Hone, I. Ellwood, M. Muno, Ari Mizel, Marvin L. Cohen, and A. Zettl, "Thermoelectric Power of Single-Walled Carbon Nanotubes" 1998, V. 80, No. 5.
[17] F. J. Blatt, Thermoelectric Power of Metals (Plenum Press,New York, 1976.
[18] K, Irma, C. Jim, C. Venkat, S. Serii "Thermoelectric Transport Through Arrays Of Carbon Nanotube Junctions"American Physical Society, APS, March Meeting 2011, March 21-25, 2011, V 28.005